Extending the tephra and palaeoenvironmental record of the Central Mediterranean back to 430 ka: A new core from Fucino Basin, central Italy

Biagio Giaccio[a,b*], Niklas Leicher[c], Giorgio Mannella[d], Lorenzo Monaco[e], Eleonora Regattieri[d,f], Bernd Wagner[c], Giovanni Zanchetta[d,a], Mario Gaeta[e], Fabrizio Marra[b], Sébastien Nomade[g], Danilo M. Palladino[e], Alison Pereira[g,h,i,j], Stephanie Scheidt[c], Gianluca Sottili[e], Thomas Wonik[k], Sabine Wulf[l], Christian Zeeden[k], Daniel Ariztegui[m], Gian Paolo Cavinato[a], Jonathan R. Dean[n], Fabio Florindo[b], Melanie J. Leng[o,p], Patrizia Macrì[b], Elizabeth Niespolo[q,r], Paul R. Renne[q,r], Christian Rolf[k], Laura Sadori[s], Camille Thomas[m], Polychronis C. Tzedakis[t]

[a] *Istituto di Geologia Ambientale e Geoingegneria, CNR, Rome, Italy*
[b] *Istituto Nazionale di Geofisica e Vulcanologia, Sezione Roma 1, Rome, Italy*
[c] *Institute of Geology and Mineralogy, University of Cologne, Cologne, Germany*
[d] *Dipartimento di Scienze della Terra, University of Pisa, Pisa, Italy*
[e] *Dipartimento di Scienze della Terra, Sapienza-Università di Roma, Rome, Italy*
[f] *Istituto di Geoscienze e Georisorse, CNR, Pisa, Italy*
[g] *Laboratoire des Sciences du Climat et de l'Environnement (CEA-CNRS-UVSQ), Université Paris-Saclay, Gif sur Yvette, France*
[h] *École Française de Rome, Rome, Italy*
[i] *UMR 7194 HNHP, Département Homme et Environnement, Muséum national d'Histoire naturelle, Paris, France*
[j] *Sezione di Scienze Preistoriche e Antropologiche, Dipartimento di Studi Umanistici, Università degli Studi di Ferrara, Ferrara, Italy*
[k] *Leibniz Institute for Applied Geophysics (LIAG), Hannover, Germany*
[l] *School of the Environment, Geography and Geosciences, University of Portsmouth, Portsmouth, UK*
[m] *Department of Earth Sciences, University of Geneva (UNIGE), Geneva, Switzerland*
[n] *Department of Geography, Geology and Environment University of Hull, Hull, UK*
[o] *Centre for Environmental Geochemistry, School of Geography, University of Nottingham, Nottingham, UK*
[p] *National Environmental Isotope Facility, British Geological Survey, Keyworth, Nottingham, UK*
[q] *Department of Earth and Planetary Science, University of California, Berkeley, USA*
[r] *Berkeley Geochronology Center, Berkeley, USA*
[s] *Dipartimento di Biologia Ambientale, University of Roma "La Sapienza", Rome, Italy*
[t] *Environmental Change Research Centre, Department of Geography, University College London (UCL), London, UK*

Abstract

Here we present the first tephrostratigraphic, palaeomagnetic, and multiproxy data from a new ~98 m-deep sediment core retrieved from the Fucino Basin, central Italy, spanning the last ~430 kyr. Palaeoenvironmental proxy data (Ca-XRF, gamma ray and magnetic susceptibility) show a cyclical variability related to interglacial-glacial cycles since the Marine Isotope Stage (MIS) 12-MIS 11 transition. More than 130 tephra layers are visible to the naked eye, 11 of which were analysed (glass-WDS) and successfully correlated to known eruptions and/or other equivalent tephra. In addition to tephra already recognised in the previously investigated cores spanning the last 190 kyr, we identified for the first time tephra from the eruptions of: Tufo Giallo di Sacrofano, Sabatini (288.0 ± 2.0 ka); Villa Senni, Colli Albani (367.5 ± 1.6 ka); Pozzolane Nere and its precursor, Colli Albani (405.0 ± 2.0 ka, and 407.1 ± 4.2 ka, respectively); and Castel Broco, Vulsini (419-490 ka). The latter occurs at the bottom of the core and has been $^{40}Ar/^{39}Ar$ dated at 424.3 ± 3.2 ka, thus providing a robust chronological constrain for both the eruption itself and the base of the investigated succession. Direct $^{40}Ar/^{39}Ar$ dating and tephra geochemical fingerprinting provide a preliminary radioisotopic-based chronological framework for the MIS 11-MIS 7 interval, which represent a foundation for the forthcoming multiproxy studies and for investigating the remaining ~110 tephra layers that are recorded within this interval. Such future developments will be contribute towards an improved MIS 11-MIS 7 Mediterranean tephrostratigraphy, which is still poorly explored and exploited.

1. Introduction

High-precision chronologies and reliable correlations of sedimentary records are fundamental requirements for reconstructing the Earth's history and evaluating the role of the processes underlying its evolution. This is particularly true for palaeoenvironmental and palaeoclimatic studies dealing with Quaternary orbital and millennial-scale variability. Our understanding of the spatial-temporal variability, magnitude, regional expressions, and underlying mechanisms of the triggering, propagation, and sustaining of past climate change is dependent on high-quality and high-resolution proxy series, provided that they are anchored to precise and accurate time scales (e.g., Govin et al., 2015). The lack of robust chronologies also limits the use of data for testing climate models, which are fundamental for understanding the climate system and forecasting future change.

Alongside the growing need of more accurate, precise, and high-resolution chronologies in sedimentary archives, the study of distal tephra has experienced an outstanding surge during the last decade (e.g., Lane et al., 2017). Diagnostic geochemical features of tephra components (e.g., glass, minerals) allow the unambiguous identification and tracking of tephra layers in different sedimentary settings, thus providing us with a unique tool to establish stratigraphic correlations between sedimentary archives (tephrostratigraphy) and to transfer radioisotopic ages of these layers (tephrochronology) over wide regions.

The relevance of tephra studies is clearly highlighted in large international projects and working groups, such as RESET (RESponse of humans to abrupt Environmental Transitions; e.g., Lowe et al., 2015) and INTIMATE (INTegration of Ice core, MArine and TErrestrial records of the Last Termination; e.g., Blockley et al., 2014), which have drawn attention and prompted the development and application of tephrochronology. Furthermore, tephrochronology has also been shown to be vital in several of the recent continental (ICDP) deep drilling projects (e.g., PASADO, Wastegård et al., 2013; PALAEOVAN, Litt and Anselmetti, 2014; SCOPSCO, Leicher et al., 2016). In spite of these efforts a satisfactory and reliable tephra framework for the Mediterranean region is available only for the 200 kyr (Bourne et al., 2010; 2015; Giaccio et al., 2012b; 2017; Insinga et al., 2014; Paterne et al., 2008; Petrosino et al., 2016; Smith et al., 2011; Sulpizio et al., 2010; Tamburrino et al., 2012; Tomlinson et al., 2014; Wulf et al., 2004; 2012; Zanchetta et al., 2008; 2018). Extending the use of tephrochronology for extra-regional to global scale chronological purposes beyond the current relatively short temporal limits of the Upper Pleistocene has thus become an urgent need.

Reliable tephrostratigraphies can be best achieved in regions characterised by: (*i*) intense and frequent Quaternary potassic-ultrapotassic explosive volcanism, that allow high-precision $^{40}Ar/^{39}Ar$ dating, and by (*ii*) the presence of nearby, long and continuous sedimentary archives that in addition to the recording of tephra provide detailed palaeoclimatic and palaeoenvironmental information. In the central Mediterranean region, the Plio-Quaternary lacustrine successions hosted in the Central-Southern Apennine intermountain tectonic depressions (e.g., Galadini et al., 2003) are among the few sedimentary archives that fulfil both these requirements. These archives record in detail the environmental and climatic history (e.g., Karner et al., 1999; Giaccio et al., 2015a; Mannella et al., 2019; Regattieri et al., 2015; 2016; 2017; 2019; Russo Ermolli et al. 2015) and contain frequently deposited tephra layers from adjacent ultrapotassic peri-Tyrrhenian, high-explosive volcanic centres that can be $^{40}Ar/^{39}Ar$ dated (e.g., Karner et al., 1999; Giaccio et al., 2012a; 2013b; 2014; 2017; Amato et al., 2014; Petrosino et al., 2014b) (Fig. 1). Among these, the Fucino Basin, located in the centre of the Central Apennines (Fig. 1), is a key archive as first studies of its uppermost lacustrine succession (<190 ka) have demonstrated the potential for retrieving a long and continuous record of both past volcanic activity and environmental changes (Di Roberto et al., 2018; Giaccio et al., 2015b; Giaccio et al., 2017; Mannella et al., 2019).

In June 2017, a new scientific drilling campaign was conducted with the aim of extending the available Fucino record back in time and of exploring its actual potential, in terms of sedimentary continuity and wealth of both tephra and palaeoclimatic proxy data. Here we present the first results of ongoing studies on the new F4-F5 core (Fig. 1) and provide a preliminary chronological and palaeoenvironmental framework for the forthcoming high-resolution, multiproxy investigations.

2. Geological, structural and stratigraphic setting of the Fucino Basin

The Fucino Basin (coordinates of the basin's midpoint: 42° 00' 00" N; 13° 30' 00" E) is located at ~650 m a.s.l and is surrounded by some of the highest peaks of the Central Apennine, which hosted mountain glaciers during glacial periods (e.g., Giraudi and Giaccio, 2015). Until recently, the Fucino Basin hosted Lake Fucinus, which covered a surface area of 150 km^2 prior to its partial drainage during the 1^{st}-2^{nd} century AD, which was completed at the end of the 19^{th} century.

The basin is bounded to the ENE by normal faults of the Fucino Fault System (FFS; Galadini and Galli, 2000). The FFS is the main, currently active, tectonic structure responsible for the Plio-Pleistocene opening and evolution of the Fucino Basin (Cavinato et al., 2002), as well as for generating high magnitude (Mw 7.0) historical earthquakes (Galli et al., 2016). Longitudinal and transverse seismic lines crossing the basin with respect to the NW-SE strike of the FFS, depict a semi-graben geometry with increasing thickness of the sedimentary infill from the west to the east (i.e., toward the FFS) and from the north-western and south-western tips of the FFS to its main depocenter, located a few km N-W of San Benedetto village (Fig. 1). Specifically, Cavinato et al. (2002) distinguished four unconformity-bounded units: Seq. 1, Meso-Cenozoic substratum, Seq. 2, Messinian, Seq. 3 Pliocene, and Seq. 4, Quaternary, separated by major unconformities A, B, and C, respectively (Fig. 1). The EW-trending seismic Line 1, crossing the depocenter of the basin, shows that Quaternary sediments, which here reach a maximum thickness of ~ 700 m, have not been significantly affected by tectonic deformation or sedimentary unconformities (Cavinato et al., 2002) (Fig. 1). During the past decades, several cores were drilled in the Fucino semi-graben basin for scientific and geotechnical purposes. So far, the 200 m-long GeoLazio core is the deepest borehole in the Fucino plain (GL in Fig. 1), but only very few data is available on its geochronological and stratigraphical aspects (Follieri et al., 1986; 1991; Giaccio et al., 2015b).

3. Material and methods

3.1. Drilling site selection strategy and procedure

The general semi-graben architecture of the Fucino Basin (Line 1, Fig. 1) was taken into account when selecting a new drilling site characterized by a lower sedimentation rate with respect to F1-F3 (~0.45 mm/yr in average, Giaccio et al., 2017; Mannella et al., 2019), i.e., potentially yielding older sediments to a relatively shallow depth. The respective site was located ~1 km east of the F1-F3 site (42°00'07"N, 13°32'19"E), in between the GeoLazio and SP cores (Fig. 1), both characterized by mean sedimentation rate of ca. 0.2 mm/yr (Giaccio et al., 2015b; 2017). In order to recover a sedimentary succession as complete as possible, two parallel cores were recovered at the same drilling site in two boreholes, F4 and F5, ca. 3 m apart. The first hole (F4) reached a field depth of 87.00 m and the second hole (F5) a depth of 87.75 m. Individual core sections had a length of 1.5 m, and both holes were drilled with an overlap of 75 cm between the respective runs, thus ensuring that any possible gap in-between two consecutive core sections of the F4 core series was likely recovered in the middle of core section of the F5 core series, and vice versa (Fig. 2). Samples from core catchers were taken directly in the field, whereas the rest of the core was stored in a dark and cool place for further analyses.

3.2. Downhole logging

Geophysical downhole logging data including natural gamma radiation (spectral gamma ray), magnetic susceptibility, resistivity, temperature, acoustic velocity, acoustic borehole televiewer, and borehole diameter and dip (borehole and strata) were measured in hole F4. Spectral gamma ray was logged first through the drill pipe and is the depth reference for all following runs. All other runs were performed under open hole condition. For that, the drill pipe was tripped out up to 67 m before logging the above-mentioned parameters separately. After finishing the logging of the interval ~80 m to 67 m, the drill pipe was pulled out to 1.5 m and the upper section was logged.

3.3. Core processing, XRF scanning and composite F4-F5 record

Sediment cores were split lengthwise and their lithology described at the Institute of Geology and Mineralogy of the University of Cologne (Germany). Immediately after core opening, one of the core halves was scanned for high-resolution images with a line-scan camera mounted on an ITRAX X-ray fluorescence (XRF) scanner (Cox Analytical Systems, Sweden). XRF scans on split core halves were made using a chromium tube set at 55 kV and 30 mA with a dwell time of 10 s and a step-size of 2.5 mm. Data processing was performed with the QSpec 6.5 software (Cox Analytical, Sweden) and data are expressed in counts per second, averaged at 25 cm intervals. Optical information derived from high-resolution line-scan imaging and XRF data were used for correlating the individual, overlapping core segments from sites F4 and F5 to create a composite core (Fig. 2). Among homologous stratigraphic intervals documented in both F4 and F5 cores, we systematically selected the more expanded one, which results in a total length of F4-F5 composite core that exceeds the depth of the individual boreholes. Sections that were obviously disturbed by the coring process were excluded from the core composite or marked as not relevant for high-resolution analyses. If unambiguous core correlation was not possible due to non-overlapping sections or larger disturbed sections, the field depth of the cores and the length of the core catcher were taken as measures to continue the core composition downward. The length of the resulting core composite, 98.11 m composite depth (mcd), exceeds the drilling field depth by 10.36 m, which is partly due to core expansion and degassing after core recovery and to the difference in the thickness of homologous stratigraphic intervals documented in the F4 and F5 core sections selected for the composite F4-F5 core.

3.4. Palaeomagnetic analyses

For palaeomagnetic analyses the natural remanent magnetisation (NRM) of the core halves was measured consecutively in 1 cm spacing by a cryogenic magnetometer (760 SRM-RF-SQUID; 2G Enterprise, USA) with an embedded alternating field demagnetizer at the palaeomagnetic laboratory Grubenhagen of the Leibniz Institute for Applied Geophysics (LIAG; Hannover, Germany). Subsequent progressive alternating field (AF) demagnetization in four equally sized steps up to 16 mT. These measurements allow for a first evaluation of the quality of the magnetic signal. The inclination values measured after the 16 mT demagnetisation step were used to show downcore variations of the direction of the palaeomagnetic field. The inclination data of core sections showing drilling induced disturbances were excluded from the interpretation, as well as the suspicious values gained from the top and the bottom of drill core segments. Since core measurements integrate the signal over approximately 12 cm, drilling induced disturbances influence the data of not affected core sections. Thereby, data gaps exceed the actual disturbed sections of the core. The magnetic susceptibility (MS) of the core halves was determined in 1 cm spacing using a 14 cm loop sensor and a VSFM control unite by Magnon GmbH (Dassel, Germany).

3.5. Tephrochronological analyses

3.5.1. Tephrostratigraphy and major element composition

Major and minor oxide element compositions were determined on micro-pumice fragments and/or glass shards of eleven selected tephra layers (Table 1) distributed along the F4-F5 succession as shown in Figure 2c. The individual layers were labelled using an alphanumeric code that identified the hole (i.e., F4 or F5), the progressive number of the section core (from 1 to 58) and the depth in cm of the top and bottom of the layer in the ~150 cm-long core section (see second column in Table 1). Then, labels were simplified using the criterion previously proposed for the F1-F3 core (Giaccio et al., 2017), i.e., the tephra have been labelled as Tephra Fucino (TF) followed by a sequential number indicating the relative stratigraphic position of each tephra, with TF-1 being the uppermost layer (Table 1).

198 Table 1: Analysed tephra layers from core F4-F5.

Fucino tephra	Sampling code	Bottom mcd	Thickness (cm)	Main lithological features	Source
TF-4	F5-8 77-93	**10.57**	15.50	Darkish coarse ash made of dense blackish porphyritic scoria including crystals of leucite, pyroxene and dark mica, also occurring as abundant loose clasts. Accessory lithic made of lava and holocrystalline clasts also occur.	Colli Albani
TF-5	F5-8 148-154	**11.13**	~6*	Darkish coarse ash made of dense blackish porphyritic scoria including crystals of leucite, pyroxene and dark mica, also occurring as abundant lose clasts. Accessory lithic made of lava and holocrystalline clast also occur.	Colli Albani
TF-7	F5-10 147-149	**14.14**	2.00	Greyish medium ash made of whitish-transparent micro-pumices associated with dense brownish glass shards with abundant lose crystals of large sanidine and black mica.	Ischia
TF-8	F5-12 90-95	**17.15**	4.50	Darkish ash made of blackish poorly vesicular scoria associated to scarce crystals of leucite and clinopyroxene.	Colli Albani
TF-12	F5-15 90-91	**21.53**	1.00	Greyish to dark yellow, fine grained ash with whitish-transparent micropumices and glass shards. Stretched/elongated vesicles, only very few loose crystals of sanidine, black mica and pyroxene.	Campi Flegrei-CVZ
TF-17	F5-20 89-91	**29.64**	2.00	Fine to coarse grained, greyish ash with 1) greyish dark vesicular scoria; 2) brownish and transparent glass shards and micropumice; 3) coarse, (rounded) whitish and greyish pumice, with loose sanidine, clinopyroxene, and amphibole crystals	Campi Flegrei-CVZ
TF-62	F4-39 90-100	**60,60**	10.00	Darkish coarse ash consisting of 1) greyish dark vesicular scoria; 2) brownish and transparent glass shards and micropumice; 3) coarse, (rounded) whitish and greyish pumice, with loose sanidine, clinopyroxene, and amphibole crystals.	Sabatini
TF-85	F5-49 74-88	**80.52**	13.25	Darkish medium-coarse ash made of both black porphyritic leucite-bearing scoriae and aphyric highly vesicular black scoriae, along with abundant crystals of leucite and dark mica and lithics. Toward the top, the ash becomes finer.	Colli Albani
TF-117	F5-57 0-7	**95.13**	7.00	Darkish fine ash made of black porphyritic leucite-bearing scoriae associated with free crystals of leucite and lithics. Toward the top, the sediment evolves into a coarse ash made of blackish vesicular porphyritic scoriae along with leucite and lithics.	Colli Albani
TF-118	F5-57 16-23	**95.29**	7.50	Darkish fine ash made of black porphyritic scoriae along with abundant free crystals of leucite and minor lithics.	Colli Albani
TF-126	F5-58 64-66	**97.24**	2.00	Light-grey medium ash made of highly vesicular white pumices associated with crystals of sanidine, plagioclase, dark mica and opaques and glass shards and minor lithics. Toward the top, the sediment turns to a dark grey-blackish medium ash.	Vulsini

199 *Base of tephra inside of the core-catcher, not in composite depth.

200

201 In addition, in order to improve the available reference datasets for robust geochemical comparisons and for
202 identifying the volcanic source of the Fucino tephra layers, we are performing new glass chemical analyses of
203 the main proximal volcanic units of Latium and Roccamonfina volcanoes, which are the main sources of the
204 Fucino Middle Pleistocene tephra. Specifically, based on the estimated ages of the F4-F5 tephras investigated
205 in this study, glass shards and micropumices of pyroclastic fall and flow units from the Castel Broco eruption,
206 Vulsini Volcanic District (e.g. Palladino et al., 2010), the Tufo Giallo di Sacrofano eruption, Sabatini Volcanic
207 District (Sottili et al., 2010) and the layer R94-30C, from Tiber River MIS 11 aggradational successions (Marra
208 et al., 2016), were analysed and are presented in this study.

209

210 Polishing and carbon coating of epoxy pucks were performed for electron microprobe analyzer wavelength
211 dispersive spectroscopy (EPMA-WDS) analysis at the Istituto di Geologia Ambientale e Geoingegneria of the
212 Italian National Research Council (IGAG-CNR, Rome), at the Institute of Geology and Mineralogy of the
213 University of Cologne (IGM-UC, Germany) and at the Geoforschungszentrum (GFZ), Potsdam (Germany).
214 At IGAG-CNR, geochemical analyses of individual glass shards were performed using a Cameca SX50 EPMA
215 equipped with a five-wavelength dispersive spectrometer, calibrated and set to the same operating conditions
216 as in previous studies (Giaccio et al., 2017). At IGM-UC, individual glass shards and reference standards were
217 measured using a JEOL JXA-8900RL EPMA equipped with a five-wavelength dispersive spectrometer, which

was set to 12 keV accelerating voltage, 6 nA beam current, and 5 µm beam diameter. Detailed settings such as counting times, measuring order, and reference materials used for calibration are given along with the supplementary material. At the GFZ, major-element compositions of single glass shards were determined using a JEOL JXA8500F EPMA. The instrument was set at an accelerating voltage of 15 kV, a 10 nA beam current, and a 3–10 µm beam with count times of 20 s for the elements Mg, P, Cl, Ti, Mn, and Fe, and 10 s for F, Na, Al, Si, K, and Ca. A range of MPI-DING reference glasses including GOR128-G (komatiite), ATHO-G (rhyolite) and StHs6/80 (andesite) (Jochum et al., 2006) as well as natural Lipari obsidian (Hunt and Hill, 1996; Kuehn et al., 2011) were employed as secondary glass standards in order to maintain inter-laboratory consistency of analytical data.

Geochemical analyses yielding analytical totals <93 wt.% were rejected, whereas all analyses with higher totals were normalized to 100% on a LOI-free basis, excluding volatiles (Cl, SO_3, and F). Glass shards and micropumices were classified according to their geochemical composition using total alkali vs. silica (TAS) diagrams (Le Bas et al., 1986).

3.5.2. $^{40}Ar/^{39}Ar$ geochronology

$^{40}Ar/^{39}Ar$ geochronology was performed at the Laboratoire des Sciences du Climat et de l'Environnement (CNRS-LSCE; Gif Sur Yvette, France). Tephra TF-126 (sample code F5-58 64-63; 97.24 m depth) was sieved and subsequently 25 pristine sanidine crystals were picked from the 300 µm to 400 µm fraction. These crystals were irradiated 2 hours in the Cd-lined, in-core CLICIT facility of the Oregon State University TRIGA reactor. After irradiation, 15 crystals were individually loaded in a copper sample holder and put into a double vacuum Cleartran window. Each crystal was then fused using a Synrad CO_2 laser at 15% of nominal power (~25 Watts). The extracted gas was purified for 10 min by two hot GP 110 and two GP 10 getters (ZrAl). Argon isotopes (^{36}Ar, ^{37}Ar, ^{38}Ar, ^{39}Ar and ^{40}Ar) were analysed by mass spectrometry using a VG5400 equipped with an electron multiplier Balzers 217 SEV SEN coupled to an ion counter. The neutron fluence J value for each sample was calculated using co-irradiated Alder Creek Sanidine (ACs-2 hereafter) standard with an age of 1.1891Ma (Niespolo et al., 2017) and the total decay constant of Renne et al. (2011). The J-value computed from standard grains is 0.00053001 ± 0.00000159. Mass discrimination was estimated by analysis of Air pipette throughout the analytical period, and was relative to a $^{40}Ar/^{36}Ar$ ratio of 298.56 (Lee et al., 2006). Procedural blank measurements are computed after every two or three unknowns, depending on the beam measured. For 10 min static blank, typical backgrounds are about 2.0-3.0 10^{-17} and 5.0 to 6.0 10^{-19} mol for ^{40}Ar and ^{36}Ar, respectively. The precision and accuracy of the mass discrimination correction was monitored by weekly measurements of air argon of various beam sizes.

For a consistent comparison of geochronological data, where possible (i.e., when monitor constant used is known and declared), all $^{40}Ar/^{39}Ar$ ages used from the literature have been recalculated relative to an age of 1.1891 Ma for the Alder Creek sanidine monitor standard (Niespolo et al., 2017), with the uncertainties expressed at 2σ.

4. Results

4.1. Borehole data

Gamma ray logging data show a trend towards lower values from the bottom to the top, and the development from shorter to longer periods from the base to the borehole top (Fig. 3b). While in the lower part several quasi-cyclic alternations with a period around 5 m can be seen in the gamma ray data, two much longer quasi-cycles from ~38-22 m and from ~22 m to the top are especially prominent. This ~20 m cyclicity can be seen also further down in the record (Fig. 3b). Cyclic behaviour can be visualized in a wavelet analysis plot using the 'biwavelet' R package (Gouhier et al., 2018; R Core Team, 2017), clearly showing the trend of longer periods towards the top (supplementary Fig. S1). The seemingly strong cyclicity at ~35 m is the result of a single peak in the data (see Figs. 2b and S1). The magnetic susceptibility shows various peaks from a base line, but the $\log_{10}$ of the magnetic susceptibility emphasizes a minor variability characterised by a quite regular cyclicity, which appears coherent with that depicted by gamma ray (Fig. 3a).

4.2. Lithology and XRF scanning calcium counts of the F4-F5 composite core

The ~98 m-long F4-F5 core composite is mainly composed of grey-whitish lacustrine calcareous marl, with a variable proportion of darkish clay. Starting from the depth of ~60 m, tephra layers become particularly frequent and thick (up to 15-20 cm), and are often surmounted by dm-thick intervals made of volcanoclastic material, likely deriving from the immediate reworking of tephra fallout in lake catchment.

Calcium represents one of the major element components of the sediments and shows large variations in XRF counts (0.15-4.60 × 10^6 cps) (Fig. 3e). Calcium has a polymodal statistical distribution, which can be divided in seven, partially overlapping, normally distributed populations (Fig. 3e). A broad population of intermediate values ($\mu \pm 2\sigma$: 2.30 ± 1.25) separates two groups consisting of three populations each and clustering in the high ($\mu \pm 2\sigma$: 4.30 ± 0.30; 3.65 ± 0.50; 3.10 ± 0.35) and in the low ($\mu \pm 2\sigma$: 2.00 ± 0.22; 1.65 ± 0.30; 1.15 ± 0.60) range of Ca counts, respectively. These two clusters depict five intervals characterized by prevailing high Ca counts intervened with four intervals with prevailing low Ca counts along the succession (Fig. 3e). The thickness of intervals with prevailing high Ca counts ranges between 4.85 and 11.80 m, while intervals with prevailing low Ca counts are thicker and range between 10.48 and 15.18 m in thickness.

4.4. Palaeomagnetic data

The palaeomagnetic data show normal direction with relative steep dipping inclination values (Fig. 3d). Because of the rotation movement during the drilling process, the cores are not oriented for the North direction and the declination cannot be taken into account. Gaps in the dataset arise from drilling induced disturbances, which have destroyed the primary direction recorded in the sediment. After cleaning the data set, conspicuous data occur around 13 mcd, 25 mcd, and 39 mcd. These sections are characterized by reversed inclination values or flat dipping normal inclination values. In contrast to the data from drilling induced disturbances, which show similar features, these changes in inclination are similarly recorded in both cores, F4 and F5. The MS of the core material was used for determination of the relative palaeointensity (RPI) by normalizing the remanent magnetization measured after the 12 mT AF demagnetization step by the MS (Tauxe, 1993). Because of very low MS values (< 15 ·10^{-6} SI) of large parts of the cores a reliable calculation of the RPI was not possible by this method.

4.5. Tephra lithology and glass composition

A total of ~130 visible tephra layers were identified in the F4-F5 composite profile during core inspection. The thickness and main lithological features of the eleven investigated and described here tephra are summarized in Table 1. Full glass compositions are provided in supplementary dataset 2 (SD 1), while their classification according to the total alkali *versus* silica diagram (TAS, Le Bas et al., 1986) is shown in Figure 3a.

In the TAS diagram the analysed tephra layers cluster in two different compositional groups (CG), represented by K-foidites of CG1, which includes six layers (TF-4, TF-5, TF-8, TF-85, TF TF-116, and TF-117), and potassic trachytes-phonolites to tephriphonolites and phonotephrites of CG2, which includes five other tephra layers (TF-7, TF-12, TF-17, TF-62, and TF-126) (Fig. 4a).

4.6. $^{40}Ar/^{39}Ar$ age of TF-126

Full analytical details for individual crystals are given in the supplementary dataset 2 (SD 2) and presented in Figure 4 as a probability diagram with the associated inverse isochron. Individual crystal age uncertainties are given at 1σ level and weighted mean age uncertainties are quoted at 2σ level. After excluding three crystals older than the main crystal age population, the remaining twelve crystals have equivalent ages within uncertainty (Fig. 4) giving a meaningful weighted mean age of 424.3 ± 3.2 ka (MSWD = 1.16, P = 0.7; Fig. 4). This age is undistinguishable within uncertainty from the inverse isochron age (i.e., 422.8 ± 3.8 ka (MSWD = 0.87). The $^{40}Ar/^{36}Ar$ initial intercept is identical within uncertainty to the atmospheric one (see SD 2), excluding an excess argon component. Therefore, the age of 424.3 ± 3.2 ka (2σ) is considered as the age of the eruption and deposition of tephra TF-126 hereafter.

5. Discussion

5.1. Palaeoclimate and preliminary chronological framework for F4-F5

The variability of Ca content in Fucino lake sediments is mainly related to variations in bio-mediated precipitation of endogenic calcite, the precipitation of which depends on the lake's primary productivity, in turn related to temperature and hydrology (e.g., Mannella et al., 2019). Based on the well constrained tephrochronology available for the F1-F3 succession (Fig. 3g), fluctuations in the Ca XRF profile have been demonstrated to express the glacial-interglacial and sub-orbital climatic variability of the last ~190 kyr, with high Ca during warm MIS 5 and MIS 1, and lower Ca during the cold MIS 6 and MIS 4-MIS 2 (Mannella et al., 2019) (Fig. 3f).

The general pattern of the major fluctuations of the Ca XRF curve recorded in the upper 35 mcd of the F4-F5 succession replicates the Ca XRF profile of the entire F1-F3 core, indicating that the two stratigraphic intervals span the same temporal interval. With the exception of some sharp and prominent spikes, clearly related to thick tephra layers, gamma ray and magnetic susceptibility signals of the upper 35 mcd of core F4-F5 fluctuate coherently with Ca counts (Fig. 3a-b). This suggests they can be considered as further proxies of the glacial-interglacial cyclicity. Indeed, low gamma ray and magnetic susceptibility are consistent with the low detrital input during warm MISs, while high levels of these parameters indicate a high detrital input consistent with colder and drier climatic conditions of the cold MISs.

The overlap of the upper 35 mcd of the F4-F5 core with the 83 m-long F1-F3 core, i.e., the last ~190 kyr indicates a sedimentation rate of ~0.2 mm/yr for F4-F5, in line with estimates from the GL (Giaccio et al., 2015b) and SP cores (Giaccio et al., 2017) located close by (Fig. 1). Additional confirmation is provided by the tephrochronological study of the cores FUC-S5-6 (Di Roberto et al., 2018), where an average of ~0.13 mm/yr for the last 56 kyr has been shown. This lower sedimentation rate is in agreement with the position of the FUC-S5-6 site, where the sedimentary wedge is expected to become thinner and the isochrones shallower (Fig. 1).

Based on this coherent stratigraphic framework, the third, fourth, and fifth intervals with relatively high concentration of Ca, and, conversely, low gamma ray and magnetic susceptibility, can be related to the MIS 7, MIS 9 and MIS 11, respectively. The chronological framework is further supported by the direct $^{40}Ar/^{39}Ar$ dating of tephra TF-126, which provides a robust age constrain for the base of the fifth and last interval with relatively high Ca content at 424.3.2 ± 3.2 ka (Fig. 3g), near the onset of MIS 11 at 424 ka based on the benthic isotope stack (Lisiecki and Raymo, 2005) (Fig. 3g) and ~426 ka based on U/Th dating from the Chinese speleothems (Chen et al., 2016). Despite this strong chronological constrain, the general shape of the Ca profile corresponding to the MIS 11 interval appears quite fragmentary with respect to a more regular trend expected for this period, as, e.g., recorded in LR04 benthic record (Fig. 3h). This might be due to both significantly changing in sedimentation rates and the occurrence of tephra layers (Fig. 3c), which are quite frequent and thick in this stratigraphic interval, that results in strong disturbances of the Ca profile that mimic climatic oscillations within MIS 11. Therefore, in order to have a reliable climatic expression of MIS 11, a detailed age model need to be developed by removing all tephra layers; a procedure which is commonly done when dealing with detailed paleoclimatic investigations (e.g., Mannella et al., 2019), but unnecessary for the purposes of this paper. We can thus use the preliminary chronological framework deriving from the correlation of the F4-F5 with the LR04 benthic record (Fig. 4; Lisiecki and Raymo, 2005) for getting a first age estimation of the tephra in the lower part (35-98 mcd) of the F4-F5 core. This provides useful, though approximate, chronological constraints for circumscribing the time interval to be consider to identify the potential equivalents of the Fucino tephra layers (Fig. 3c). For this purpose, we considered the position of the F4-F5 tephras in Ca profile to evaluate their climatostratigraphic context within the record of the LR04 benthic stack, and thus to estimate their age according to LR04 chronology assuming a conservative uncertainty of ca. ± 5 ka (Fig. 3g).

5.2. Palaeomagnetic data of F4-F5

In comparison to the ~58° inclination of today's earth magnetic field in the Fucino Basin, the determined inclination values of the palaeomagnetic field of the sediments from F4-F5 cores are frequently too steep (Fig. 3d). The deviation may arise from slight deformations of the material during the coring process, just as by considering the inclination of the 16 mT AF step instead of evaluating the characteristic remanent magnetisation (ChRM). However, downcore changes of the palaeomagnetic field show sections with conspicuous values around 13 mcp, 25 mcp, and 39 mcp. According to the age constrains provided by tephrochronology, these features coincide with the positions expected for the geomagnetic excursions Laschamp (40-41 ka), Blake (~120 +/- 12 ka), and Iceland Basin (189-192 ka), respectively (Channell, 2006; Channell 2014; Singer et al., 2014; Vasquez and Lidzbarski 2012). This result suggests the Fucino Basin to host an outstanding magnetic record and justifies the planed very time-consuming detailed study of discrete samples, necessary to consider the ChRM.

5.3. Volcanic sources of tephra layers from core F4-F5

The Fucino Basin is located at a relatively short distance from the peri-Tyrrhenian and the insular Quaternary Italian volcanic centres (i.e., ~100 km to some hundreds of km; Fig. 1) that were subjected to intense and frequent explosive activity during the Quaternary (e.g. Peccerillo, 2017). Hence, these volcanic centres represent the most likely sources for the Fucino tephra layers. The geochemical composition of CG1 (Fig. 4a) tephra layers is unusual within the framework of the Italian Quaternary volcanism since large explosive eruptions fed by K-foiditic magma were rare and characteristic of only few volcanic centres (e.g. Peccerillo, 2017). Among these, the Colli Albani volcanic district was the most productive source of foiditic distal tephra in Central Mediterranean area (e.g. Giaccio et al., 2013a; Giaccio et al., 2014; Giaccio et al., 2017; Leicher et al., 2016; Petrosino et al., 2014b).

The glass geochemical compositions of CG2 (potassic trachytes-phonolites to tephriphonolites and phonotephrites) tephra layers are instead shared by a number of volcanic districts and centres ranging from the northern Latium to the Campanian regions (e.g., Peccerillo, 2017) (Fig. 1), making the identification of their specific volcanic source challenging. However, the CaO/FeO vs Cl diagram (Giaccio et al., 2017) can help to discriminate between their different sources (Fig. 4b). Thus, layer TF-7 can be referred to Ischia, layers TF-12/-17 to Campi Flegrei, and layer TF-126 to the Latium volcanoes, including Vico, Vulsini and Sabatini (Fig. 4b). The source of the remaining tephra TF-62 is more complicated to define, as its composition falls at the boundary between the Roccamonfina >450 ka and Latium volcano fields (Fig. 4b). However, based on the stratigraphic position of TF-62 within late MIS 9 (~280-300 ka, Fig. 3g-h), it can be better ascribed to the Latium volcanoes than to Roccamonfina, as, at the current state of knowledge, the products from Raccomonfina <450 ka have a distinctly higher content of Cl and a lower CaO/FeO ratio (Fig. 4b). Furthermore, at the same content of Cl, tephra TF-62 shows a relatively high and wide variability of the CaO/FeO ratio (1.0 to 1.5, Fig. 4b), which, among the Latium volcanoes, is distinctive of the products from the Sabatini Volcanic District. Therefore, layer TF-62 can be more likely referred to the Sabatini activity. A summary of the source attribution of all investigated tephra is reported in Table 1.

5.4. Individual tephra correlation

5.4.1. Tephra layers between 0-35 mcd of core F4-F5, equalling 0-83 mcd of the F1-F3 core

A total of six chemically analysed tephra layers occurring within the upper 35 mcd in the new F4-F5 core can be directly linked to already identified tephra layers from the F1-F3 core. These include tephras TF-4, TF-5, TF-7, TF-8, TF-12 and TF17 (Giaccio et al., 2017), which have been allocated to volcanic sources from the Campanian and Roman areas and which are described in the following in more detail.

5.4.1.1. Tephra from Colli Albani (GC1)

F5-8 77-92 (10.56 mcd; TF-4) and F5-8 148-154 (11.13 mcd; TF-5) – these two tephra layers, belonging to the K-foidite CG1 tephra group that is attributed to the Colli Albani activity, share similar lithological features (Table 1) and heterogeneous glass compositions within the foidite field (Fig. 4a). Comparable lithological and geochemical features have been found in layers TF-4 and TF-5 in the F1-F3 record (Fig. 6a-b), which were

correlated by Giaccio et al. (2017) to the Albano 7 (35.8 ± 1.2 ka) and Albano 5 units (38.7 ± 1.6 ka, Freda et al., 2006; Giaccio et al., 2009; 2017; Mannella et al., 2019), respectively (Fig. 3f). In addition, the climatostratigraphic position of the two foiditic layers in F4-F5 within MIS 3 is similar to that of TF-4 and TF-5 (Fig. 3d-e), hence strongly supporting their correlations with TF-5/Albano 7 and TF-4/Albano 5. In the F4-F5 record, TF-4 is characterized by two coarse ~4.2 and 7.2 cm-thick levels separated by 5 cm of fine ash and lacustrine sediments, a lithological feature that is not observed in F1-F3. However, a similar lithological bifurcation of the tephra related to the most recent activity of the Albano maar, has been found in cores FUC-S5-6 (Di Roberto et al., 2018). The two levels of coarse-grained ash were interpreted by the authors as separate units and correlated to the last two eruptions of Albano maar, namely Albano 7 and 6. However, in the eastern sector of Colli Albani, where the mid-distal occurrences of the Albano eruptions are well documented, only four fallout units, related to Albano 1, 3, 5, and 7 can be recognised (Giaccio et al., 2007). The lack of the Albano units 2, 4, and 6 in the eastern, mid-distal sectors of the volcano, indicates the moderate intensity of the eruptions and their restricted dispersal, with respect to the widespread Albano units 1, 3, 5, and 7. Thus, it is rather unlikely that tephra of the Albano 6 eruption has reached the Fucino Basin and would show comparable thicknesses and grain sizes as tephra from the largest Albano 7 eruption. Therefore, the two coarser sub-layers forming TF-4 can be more likely correlated to the two main fallout sub-units (DU4b and DU4c), that form the succession of the Albano 7 unit in mid-distal area (Giaccio et al., 2007). Alternatively, they could be the result of a basal fallout (basal sub-layer) that was followed by immediate reworking of primary deposits (upper sub-layer).

F5-12 90-95 (TF-8, 17.16 mcd) – the foiditic composition of F5-12 90-95 is distinctly more homogenous compared to the above discussed TF-4 and TF-5 tephra layers (Fig. 6c). This geochemical feature is comparable with the glass composition of tephra layer TF-8 in core F1-F3 (Fig. 6c), which is correlated to the Albano 3 unit and dated between 68.7 ± 2.2 ka and 72.5 ± 3.2 ka (Freda et al., 2006; Giaccio et al., 2009). The correlation of F5-12 90-95 with TF-8/Albano 3 is also supported by the similar climatostratigraphic position that the two tephra have in the respective records at the end of the MIS 5 period (Fig. 3e-f).

5.4.1.2. Tephra from Ischia (GC2)

F5-10 147-149 (14.14 mcd; TF-7) – The ages of this Ischia tephra is constrained by the overlying TF-5 and underlying TF-8 tephra between ~40 ka and ~70 ka, (Fig. 5f-g). The trachytic glass composition of F5-10 147-149 matches that of tephra TF-7 (Fig. 7a) which is in a similar climatostratigraphic position within MIS 4 in composite core F1-F3 (Fig. 3d-e) and directly $^{40}Ar/^{39}Ar$ dated at 55.9 ± 1.0 ka (Giaccio et al., 2017). TF-7 has been correlated to the marine Y-7 tephra (Giaccio et al., 2017), a widespread Mediterranean marker tephra (Tomlinson et al. 2014), deriving from the Ischia eruption of the Monte Epomeo Green Tuff ($^{40}Ar/^{39}Ar$ age: 55.0 ± 4.0 ka, Sbrana and Toccaceli, 2011). Furthermore, the occurrence of the Y-7 tephra is also recorded in Fucino cores FUC-S5-6 (Di Roberto et al., 2018).

5.4.1.3. Tephra from Campi Flegrei (GC2)

F5-15 90-91 (21.53 mcd; TF-12) – this tephra is located in a climatostratigraphic position similar to tephra layers TF-12 and TF-13 of the F1-F3 record, i.e., close to the onset of an abrupt increase in Ca content occurring in the middle part of MIS 5 (Fig. 3e-f). TF-12 and TF-13 have been correlated to the widespread marine tephras X-5 and X-6, respectively (Giaccio et al., 2017). Although X-5 and X-6 were generated by two, temporally closely spaced eruptions of the same volcanic source – likely palaeo-Campi Flegrei or the Campanian Volcanic Zone – as shown in Figure 6b, they are quite well distinguishable solely on the basis of major element composition. The geochemical comparison with both layers (Fig. 7b) suggests that tephra F5-15 90-91 matches best the composition of TF-12/X-5. The X-5 tephra has been also identified as POP3 equivalent in the Sulmona lacustrine succession in central Italy where it is $^{40}Ar/^{39}Ar$ dated at 105.6 ± 3.0 ka (Giaccio et al., 2012b). A newer and more precise $^{40}Ar/^{39}Ar$ dating of X-5 at 105.5 ± 0.5 ka derives from the Tyrrhenian Sea (Petrosino et al., 2016).

F5-20 89-91 (29.65 mcd; TF-17) – on the basis of climatostratigraphic correlation between the F4-F5 and the chronologically well constrained F1-F3 record, tephra F5-20 89-91 can be placed into the MIS 6 period (Fig. 3e). Geochemically, it is characterised by a wide composition with SiO_2 content ranging between 48 and 61 wt%. In the F1-F3 succession, the only Campi Flegrei tephra showing the same geochemical variability and climatostratigraphic position is TF-17 (Figs. 2e-f and 6c). TF-17 has been $^{40}Ar/^{39}Ar$ dated at 158.3 ± 3.0 ka (Giaccio et al., 2017). Amato et al. (2018), on the basis of geochronological and geochemical data, identified TF-17 as the distal counterpart of the Taurano Ignimbrite from the Campanian Volcanic Zone (CVZ), which has an $^{40}Ar/^{39}Ar$ age of 160.1 ± 2.0 ka (De Vivo et al., 2001).

5.4.2. Tephra layers in the newly explored interval 35-98 mcd of core F4-F5

Five out of ~110 visible tephra layers within the newly extended interval between 35-98 mcd of core F4-F5 have been chemically characterised and correlated with Roman volcanoes based on published and new glass data from proximal tephra deposits.

5.4.2.1. Tephra from Colli Albani (GC1)

F5-49 74-88/TF-85 (80.52 mcd), F5-57 0-7/TF-117 (95.13 mcd) and F5-57 18-22/TF-118 (95.29 mcd) – based on geochronological constraints – i.e., the tephrostratigraphic correlation between the successions of F4-F5 and F1-F3, the general climatostratigraphic pattern of F4-F5, and the $^{40}Ar/^{39}Ar$ dating of the tephra TF-126 – and the typical foiditic glass composition tephra layers TF-85 (F5-49 74-88), TF-117 (F5-57 0-7) and TF-118 (F5-57 18-22) can be related to activities of the Colli Albani volcanic district. Specifically, theses layers refer to the middle-late stage of the 'Tuscolano-Artemisio' (~561-351 ka, Karner et al., 2001) or 'Vulcano Laziale' phase (Giordano et al., 2006). This phase is the most significant in terms of erupted volumes and intensity of the Colli Albani eruptive history, and comprises several caldera-forming eruptions, the products of which have been widely dispersed in the central-southern Apennines (Giaccio et al., 2013a; Giaccio et al., 2013b; Giaccio et al., 2014; Petrosino et al., 2014b) and in the Balkans (Leicher et al., 2016). Furthermore, tephra glasses from each one of the major units belonging the Tuscolano-Artemisio phase, have a quite distinctive major element composition, making their discrimination and identification unambiguous (Giaccio et al., 2013a).

The significant thickness and the relatively coarse grain-size of TF-85 (Table 1) are consistent with a large explosive eruption, which, based on the climatostratigraphic position of TF-85 in core F4-F5, occurred during MIS 10, roughly between 350-375 ka (Fig. 3d-f). In this time-period was the Villa Senni eruption, the most recent caldera-forming event of the Tuscolano-Artemisio phase, dated at 364.0 ± 4.0 (Marra et al., 2009) and 369 ± 4.2 ka (Marra et al., 2019). The major element glass composition of tephra TF-85 matches that of the glassy scoria from the proximal Villa Senni unit and its distal equivalent tephra PAG-t4, from Paganica-San Demetrio Basin, central Italy, dated to 368.0 ± 2.0 ka (Giaccio et al., 2012a) (Fig. 8a). TF-85 can be thus confidentially correlated to the Villa Senni eruption.

Tephra TF-117 (95.13 mcd) is characterized by a noticeable thickness of 7 cm and a coarse grain-size, suggesting again a large Colli Albani explosive eruption. Based on its climatostratigraphic position and being located ~3 m above the $^{40}Ar/^{39}Ar$ dated TF-126, this eruption occurred early in MIS 11, at ~400-420 ka (Fig. 3d-f). The estimated high eruption magnitude and the supposed age of TF-117 are compatible with the penultimate large eruption of the Tuscolano-Artemisio phase; i.e., the Pozzolane Nere eruption dated at 405 ± 2 ka (Marra et al., 2009). Comparisons of the geochemical composition of TF-117 with that of the proximal Pozzolane Nere equivalents confirm the correlation (Fig. 8b). Specifically, the 2 cm-thick basal unit of TF-117 (sample F5-57 5-7; Table 1) shows a more homogenous composition with respect to the more scattered composition of the overlying, 5-cm-thick and coarser sub-unit (sample F5-57 0-5; Table 1), which matches very well that of the basal Plinian fall-out of the Pozzolane Nere (Marra et al., 2009). Therefore, the basal, finer and geochemically more homogeneous sub-layer of TF-117 ($TF\text{-}117_{0\text{-}2}$) can be related to the basal Plinian fallout Pozzolane Nere, and consequently the uppermost, coarser and geochemically more scattered sub-layer

TF-117_{2-7} should represent the co-ignimbrite ash fall. However, because of strong post-depositional, zeolitization processes (Marra et al., 2009), no glass chemical data is currently available for the proximal pyroclastic flow deposits of the Pozzolane Nere for directly compare with the composition of tephra TF-117_{2-7}. The composition of the TF-117_{2-7} thus provides the first geochemical data for the pyroclastic flow deposits of the Pozzolane Nere eruption, which in terms of erupted volume represents the main stage of the eruption.
TF-118 layer (95.29 mcd) has a comparable thickness (ca. 7 cm) to that of TF-117/Pozzolane Nere (Table 1), but its finer grain, which could be due to either a significantly smaller magnitude of the explosive event or a different shape and direction of the dispersion axis. It is separated from the overlying TF-117/Pozzolane Nere (95.13 m) by only 12 cm of lacustrine sediments (Fig. 3c; Table 1), indicating that TF-118 shortly preceded the Pozzolane Nere eruption. Pereira et al. (2018) recognized a new Colli Albani eruption just below the Pozzolane Nere units; the Fontana Ranuccio 2 fallout, dated at 407.1 ± 4.2 ka (2σ analytical uncertainties) and interpreted as a Pozzolane Nere precursor. Fontana Ranuccio 2 fallout is therefore a good candidate for correlating with TF-118, immediately below the TF-117/Pozzolane Nere tephra, a hypothesis that is quite well supported by its glass composition (Fig.7c). However, as the geochemical matching is not perfect, especially for SiO_2 content, the correlation of TF-118 with Fontana Ranuccio 2 has to be considered as a tentative. The age of this Pozzolane Nere precursor is statistically indistinguishable from the age of the Pozzolane Nere, but it is slightly different in its geochemical composition (Pereira et al., 2018; Fig. 8c), making the discrimination of these two sub-contemporaneous eruptions viable.
In summary, the stratigraphic order, the lithological and geochemical features and general climatostratigraphic and geochronological settings available for the three foiditic layers TF-85, TF-117 and TF-118 define an overall coherent and robust framework supporting their correlation with Villa Senni, Pozzolane Nere, and, likely, Fontana Ranuccio 2 eruptions from Colli Albano volcano, respectively.

5.4.2.2. Tephra from the Sabatini volcanic district (GC2)
F4-39 90-100/TF-62 (59.89 mcd) – by considering its relatively large thickness (10 cm), coarse grain-size (Table 1) and phonolitic glass composition, tephra TF-62 likely derived from a large explosive eruption from the Sabatini volcanic district. Layer TF-62 occurs in the late part of the MIS 9 period, roughly at 300-280 ka (Fig. 3f). Thus, it is chronologically consistent with the early stages of the Sacrofano Caldera phase, which took place in the eastern sector of the Sabatini Volcanic District (SVD) at ~300-200 ka, and the near-contemporaneous Bracciano Caldera phase, which occurred in the central area of SDV at ~325-200 ka (Sottili et al., 2010).
The Sacrofano Caldera phase is dominated by diffuse Strombolian and hydromagmatic activity and subordinate Plinian to sub-Plinian events, among which the Tufo Giallo di Sacrofano (288.0 ± 2.0 ka, Sottili et al., 2010) and the Magliano Romano Plinian fall (313.0 ± 2.0 ka, Sottili et al., 2010) stand out as the major, caldera forming eruptions.
The Bracciano Caldera phase was similarly characterized by strombolian, effusive, and hydromagmatic activity, but also by the occurrence of some large explosive events, including the main caldera forming eruptions of the Tufo di Bracciano Unit (324.0 ± 2.0 ka, Pereira et al., 2017), the Tufo di Pizzo Prato (251.0 ± 16.0 ka, Sottili et al., 2010), and the latest Tufo di Vigna di Valle (196.0 ± 7.0 ka, Sottili et al., 2010) pyroclastic flow-forming eruptions.
The best candidate for a correlation of TF is the large caldera forming eruption of the Tufo Giallo di Sacrofano (TGDS), as its large magnitude fit with the relatively thick and coarse TF-62 and its age is close to the estimated age of TF-62 (~280-300 ka; Fig. 3g). In the TAS diagram and other selected bi-plots, the glass chemical composition of TGDS shares with the predominant (~65% of the analysed glass particles), most evolved component of the TF-62 the alkali and SiO_2 content (~15-16 wt% and 56-58 wt%), a peculiar high Al_2O_3 content (20.5-21.5 wt%) (Fig. 9a), and a very low MgO content (0.15 wt%) (Table S1). In summary, with the exception of the K_2O/Na_2O ratio, which is higher in TGDS with respect to TF-62 (Table S1), the content of all other major and minor elements of the most evolved component of the TF-62 matches very well the TGDS

559 glass composition (Table S1). Therefore, the TGDS is indicated as the most probable proximal counterpart for
560 TF-62, giving an age of 288.0 ± 2.0 ka to this latter.
561
562 5.4.2.3. Tephra from the Vulsini volcanic district (GC2)
563 **F5-58 64-66/TF-126 (97.24 mcd) –** the $^{40}Ar/^{39}Ar$ age directly determined on tephra TF-126 (424.3 ± 3.2 ka,
564 Fig. 4), restricts the chronological range of the potential equivalent to the narrow interval of ~421-428 ka.
565 Based on its phonolitic composition and the CaO/FeO vs Cl diagram either the Vulsini, Vico, or Sabatini
566 volcanic districts can be potential sources of this tephra (Fig. 5b).
567 The Southern Sabatini phase (~500 to ~400 ka, Marra et al., 2014) was the most intense one in terms of
568 explosivity and magnitude of the eruptive history of Sabatini Volcanic District (Sottili et al., 2004). However,
569 no significant eruption has been recognized so far between the Plinian Fall F dated to 449.0 ± 7.0 ka (Marra et
570 al., 2014) and the following minor activity of the San Abbondio Ash-lapilli Succession, dated to 391.0 ± 4.0 ka
571 (Marra et al., 2014). Therefore, at the present state of the knowledge, a Sabatini origin for TF-126 appears
572 unlikely.
573 The earliest activity of Vico volcano, the Vico Period I (Perini et al., 2004) of ~400-420 ka (Barberi et al.,
574 1994) was also characterized by an intense explosive activity and by the occurrence of two Plinian eruptions,
575 named Vico α and Vico β (Cioni, 1987; Laurenzi and Villa, 1987). Unfortunately, only whole-rock
576 geochemical composition are available for the proximal units of Vico Period I at present, which are not fully
577 suitable for a reliable chemical comparison with tephra glass composition. Glass geochemistry is however
578 available for some tephra attributed to Vico Period I found in distal settings of Rome are, Tuscany region,
579 Sulmona Basin and Lake Ohrid (Bigazzi et al., 1994; Marra et al., 2014; 2016; Regattieri et al., 2016; Kousis
580 et al., 2018), and that thus likely represent the main explosive eruptions of this Vico phase. All these studies
581 indicate that the most widespread tephra of Vico Period I are unusual with respect to the most common
582 compositions of the Latium ultrapotassic rocks (i.e., trachyte, phonolite, tephriphonolite), as they are
583 characterized by a trachytic-rhyolitic bimodal composition, with a distinctive rhyolitic component being often
584 the dominant or even the sole one. In combination with the slightly older age than Vico Period I, the lack of a
585 rhyolitic population in TF-126 would rule out Vico as a possible source of TF-126 tephra.
586 The upper part of the Bieadano Synthem of the Vulsini Volcanic District, spanning the late MIS 12-MIS 10
587 period, and thus encompassing the age of TF-126, comprises at least three Plinian falls. The Ponticello Pumices
588 (352.0 ± 4.0 ka), the Pumice Fallout 0 (381.0 ± 9.0 ka), and the Castel Broco eruptions (Palladino et al., 2010).
589 Of these, only Castel Broco is chronologically consistent with TF-126, although no direct age determination is
590 available for pyroclastic units of this eruption. Castel Broco deposits are in fact found below a Vico α, dated
591 to 419.0 ± 3.0 ka (Laurenzi and Villa,1987), and above the Piano delle Selva Ignimbrite, which is substantially
592 younger than ~490 ka (Palladino et al., 2010 and references therein). The major element chemical composition
593 of glass from both Plinian and pyroclastic flow units of Castel Broco succession match quite well that of TF-
594 126 (Fig. 9b). Though the wide age range of Castel Broco eruption does not allow a precise chronological
595 confirmation, the chemical composition strongly supports the correlation of TF-126 with Castel Broco, which
596 thus could be indirectly, but precisely, dated at 424.3 ± 3.2 ka.
597 As far as the potential distal equivalents are concerned, the age of TF-126 is statistically indistinguishable from
598 those of the following three tephra: (*i*) R94-30C, from Roma costal area, which marks the glacial termination
599 V in MIS 12-MIS 11 aggradational successions of the Tiber River, yielding a $^{40}Ar/^{39}Ar$ age of 423.4 ± 5.0 ka
600 (Marra et al., 2016); (*ii*) OH-DP-1733, from Lake Ohrid succession, which is stratigraphically located at the
601 MIS 12-MIS 11 transition of the Lake Ohrid palaeoclimatic records, with a modelled age of 422.3 ± 6.1 ka
602 and attributed to the Roccamonfina volcano (Leicher et al., in review); and (*iii*) MOL 13, from Bojano Basin,
603 southern Italy, dated by $^{40}Ar/^{39}Ar$ method at 427.3 ± 6.0 ka and related to Rio Rava phase activity (550-358
604 ka; Rouchon et al., 2008) of the Roccamonfina volcano (Amato et al., 2014).
605 However, certain differences in glass composition do not support a correlation of the three Roman, Bojano and
606 Ohrid tephra, neither among them nor with TF-126 tephra (Fig. 9b). This highlights a quite complex framework

of the central Mediterranean tephrostratigraphy during the MIS 12-MIS 11 transition (cfr. Leicher et al., in review), indicating the occurrence of several temporally closely spaced eruptions from multiple peri-Tyrrhenian volcanic sources, including Vulsini (Castel Broco/TF-126), Roccamonfina (post-Rio Rava, MOL 13 and OH-DP-1733) and at least another currently undetermined volcano (R94-30C, Vico?).

5.5. The composite Fucino tephra record and preliminary age model

5.5.1. F1-F3/F4-F5 composite tephra record spanning the last 430 kyr

The recognition of tephra TF-4, TF-5, TF-7, TF-8, TF-12, and TF-17 in the F4-F5 record, shared with the previously investigated core F1-F3, allows a robust synchronization of the two records along six tie points (Fig. 10). Moreover, the high-resolution XRF Ca profiles of the F1-F3 and F4-5 successions enable further refinement of the correlation using the high-frequency variability of this element as an aligning tool (Fig. 9), which allows us to transfer, on the basis of the tephra stratigraphic order and climatostratigraphic position, all F4 tephra in F5 record, and vice versa (Fig. 10). This results in a composite F1-F3/F4-F5 record of 134 tephra that would make Fucino Basin the richest archive of the peri-Tyrrhenian explosive volcanism continuously spanning over the last 430 kyr.

Significantly, the new F4-F5 composite record improves the general tephrostratigraphic framework, not only for the previously unexplored temporal interval of ~190-430 ka (Fig. 11), but also for the interval spanning the last 190 kyr (Fig. 10). Indeed, the combination of the F1-F3 and F4-F5 cores adds seven new tephra in the 190 ka-present interval that apparently were not documented in core F1-F3, because of either drilling issues and/or the possible lenticular geometry of the tephra beds. Four of these new tephra layers are situated in a MIS 3-MIS 4 interval between TF-7 (Y-7, ~56 ka) and TF-8 (~70 ka), one at the onset of MIS 5, just below TF-14 (Sabatini, 126.0 ± 1.0 ka), and two in MIS 6, preceding TF-17 (Taurano Ignimbrite, 159.4 ± 1.6 ka) (Figs. 10 and 11).

However, the major contribution of the F4-F5 record in building the new composite Fucino tephra record is represented by its lowermost interval between 35-98 mcd. F4-F5 enables us to extend the Fucino record back to 430 ka, with more than 100 tephra spanning the MIS 7-MIS 11 or 190-430 ka interval (Fig. 11). Indeed, within the framework of the central Mediterranean tephrostratigraphy, the MIS 7-MIS 11 interval is among the lesser documented and known. Many of the terrestrial or marine records of this region span either younger (e.g., Monticchio: Wulf et al., 2004; 2012; San Gregorio Magno; Munno and Petrosino, 2007; Tyrrhenian Sea: Paterne et al., 2008; Adriatic Sea: Bourne et al., 2010; Bourne et al., 2015; Ionian Sea; Insinga et al., 2014) or older, and also discontinuous, intervals (Acerno Basin: Petrosino et al., 2014b; Mercure Basin: Giaccio et al., 2014; Petrosino et al., 2014a; Sulmona Basin: Giaccio et al., 2015b). Furthermore, other long continuous successions spanning the MIS 7-MIS 11 period are located too far from the highly productive peri-Tyrrhenian volcanic sources (e.g., Lake Ohrid: Leicher et al., 2016; in review; Tenaghi Philippon: Vakhrameeva et al., 2018; Vakhrameeva et al., 2019) for recording the bulk of their history and the wide gamma of their explosive intensity, including eruptions of moderate magnitude. With ~110 tephra layers distributed in the MIS 7-MIS 11 interval, the composite F1-F3/F4-F5 record has thus the potential for filling the gap of knowledge for this interval of the central Mediterranean tephrochronology.

5.5.2. Preliminary age model for the F1-F3/F4-F5 composite record

The directly $^{40}Ar/^{39}Ar$ dated tephra TF-126 (424.3 ± 3.2 ka, correlated to Castel Broco Plinian eruption from Vulsini), and the ages transferred by geochemical fingerprinting from prominent eruptions of known age (Pozzolane Nere precursor ~407 ka, Pozzolane Nere ~405 ka, Villa Senni ~368 ka and Tufo Giallo di Sacrofano ~288 ka) provide a first chronological fundation for the MIS 7-MIS 11 period. Together with the well-established chronology for the last 190 kyr (Giaccio et al., 2017; Mannella et al., 2019), this chronological information allows us to develop a first age model for the entire F1-F3/F4-F5 Fucino composite record (Fig. 12). The resulting age-depth curve for the newly explored interval is consistent with that previously established for the first 190 kyr, determined for core F1-F3 and now merged in the composite F1-F3/F4-F5 record (Fig. 12). This preliminary tephra-based age-model substantially refines and consolidates the initial chronology for

656 the MIS 7-MIS 11 inferred from the palaeoenvironmental variability (Fig. 3), which appears fully coherent
657 with both orbital and millennial-scale climatic fluctuations of the MIS 11-MIS 7 period, as shown by the
658 comparison with the sea surface temperature fluctuations on the Iberian Margin (Rodrigues et al., 2017; Fig.
659 12). The same age-model is also consistent with the known chronology for the Laschamp (40-41 ka), Blake
660 (~120 +/- 12 ka), and Iceland Basin (189-192 ka) geomagnetic excursions, as preliminarily recognised in
661 Fucino sedimentary archive (Fig. 12). Future investigations of discrete samples will permit to verify the
662 occurrence of these geomagnetic excursions and likely contribute to detail their dynamics and age.
663 Though we are aware of its preliminary state, such a chronological framework of the Fucino composite record
664 is important for the forthcoming development of tephra and proxy investigations of Fucino cores, and,
665 consequently, for getting high-resolution and fully independently dated tephrochronological,
666 palaeonvironmental and palaeomagnetic records.
667
668 **6. Summary and concluding remarks**
669 This paper presents the first results of ongoing multiproxy investigations on a new ~98 m-long sediment core
670 (F4-F5) retrieved from the Fucino Basin, central Italy. Concordant palaeoenvironmental (calcium XRF
671 scanning data from core F4-F5 and gamma ray and magnetic susceptibility data from F4 downhole logging)
672 and tephrochronological data (WDS-EMPA major element compositions and $^{40}Ar/^{39}Ar$ dating) consistently
673 indicate that new F4-F5 succession extends the previously established 190 kyr-long tephrostratigraphic and
674 palaeoeonvironmental records from the F1-F3 succession, back to 430 ka. Specifically, major element
675 composition of the glass from eleven selected out of the ~130 macroscopically visible tephra layers that occur
676 in the F4-F5 record, as well as new geochemical data from two proximal pyroclastic units of the Vulsini and
677 Sabatini volcanic districts, enabled us to correlate them to known eruptions and/or tephra units, either already
678 previously recognised in the 0-190 ka interval of F1-F3 (Albano 7, Albano 5, Albano 3, Y-7, X-5, and Taurano
679 Ignimbrite) or identified in the 200-430 ka interval for the first time. These latter are: TF-62, correlated to the
680 Tufo Giallo di Sacrofano caldera-forming eruption, from Sabatini (288 ± 2 ka); TF-85, correlated to Villa
681 Senni caldera-forming eruption, Colli Albani (367.5 ± 1.6 ka); TF-117 and TF-118, correlated to the Pozzolane
682 Nere caldera-forming eruption and its precursor, Colli Albani (405 ± 2 ka, and 407 ± 4.2 ka, respectively); and
683 TF-126, correlated to Castel Broco Plinian eruption, Vulsini (419-490 ka). In particular, TF-126 has been here
684 $^{40}Ar/^{39}Ar$ dated at 424.3 ± 3.2 ka, thus providing a direct chronological constrain for the base of the core F4-
685 F5 and a first indirect, but much more precise, age for the poorly constrained Castel Broco Plinian eruption.
686 Through tephra synchronizations, supported by palaeoenvironmental proxy alignments, we combine the F1-
687 F3 and F4-F5 records in a composite F1-F3/F4-F5 tephra record. With its ~130 ash layers spanning the last
688 430 ka, the Fucino lacustrine succession is confirmed to be the most promising sedimentary archive for getting
689 a long, continuous and rich record of stratigraphically ordered tephra of the whole Mediterranean area. Future
690 developments of the ongoing investigations of the F4-F5 sedimentary cores are unavoidably intended to
691 expand the potential of the Fucino succession as a key, reference tephrochronological record, at the service of
692 a wide spectrum of the Quaternary sciences, including palaeoclimatology, palaeomagnetism, archaeology,
693 Quaternary geology, active tectonics and volcanology, on a geographic scale that extends from local to extra-
694 regional.
695
696 **Acknowledgements**
697 This article is a contribution of project "FUcino Tephrochronology Unites Quaternary REcords (FUTURE)",
698 supported by the Italian Ministry of Education, University and Research (MIUR, grant PRIN No.
699 20177TKBXZ_003; G. Zanchetta, coordinator). The $^{40}Ar/^{39}Ar$ age was supported by the CNRS INSU LEFE
700 action to S. Nomade. An international consortium, including IGAG-CNR, IGG-CNR, University of Pisa,
701 University of Cologne, INGV-Roma, University of Rome La Sapienza, LIAG-Hannover, University of
702 Geneva, University of Nottingam, provided the funding for supporting the 2017 Fucino drilling campaign. We

703 thank Antonello Provenzale for the additional financial support offered for sustaining drilling campaign. The
704 Fucino project is co-funded by DFG (German Research Foundation) grant WA 2109/16
705
706 Two anonymous reviewers provided thoughtful and constructive comments that improved the manuscript.
707
708

709 **References**

710 Amato, V., Aucelli, P.P.C., Cesarano, M., Filocamo, F., Leone, N., Petrosino, P., Rosskopf, C.M., Valente, E., Casciello, E., Giralt, S.,
711 Jicha, B.R., 2018. Geomorphic response to late Quaternary tectonics in the axial portion of the Southern Apennines (Italy): A
712 case study from the Calore River valley. Earth Surface Processes and Landforms 43, 2463-2480.
713 Amato, V., Aucelli, P.P.C., Cesarano, M., Jicha, B., Lebreton, V., Orain, R., Pappone, G., Petrosino, P., Ermolli, E.R., 2014. Quaternary
714 evolution of the largest intermontane basin of the Molise Apennine (central-southern Italy). Rendiconti Lincei 25, 197-216.
715 Barberi, F., Buonasorte, G., Cioni, R., Fiordelisi, A., Foresi, L., Iaccarion, S., Laurenzi, M.A., Sbrana, A., Verenia, L., Villa, I.M.,
716 1994. Plio-Pleistocene geological evolution of the geothermal area of Tuscany and Latium. Memorie Descrittive della Carta
717 Geologica d'Italia 49, 77-134.
718 Bigazzi, G., Bonadonna, F., Cioni, R., Leone, G., Sbrana, A., Zanchetta, G., 1994. Nuovi dati geochimici, petrografici e geocronologici
719 su alcune cineriti Plio-Pleistoceniche del Lazio e della Toscana. Memorie descrittive della Carta Geologica d'Italia 49, 135-
720 150.
721 Blockley, S.P.E., Bourne, A.J., Brauer, A., Davies, S.M., Hardiman, M., Harding, P.R., Lane, C.S., MacLeod, A., Matthews, I.P., Pyne-
722 O'Donnell, S.D.F., Rasmussen, S.O., Wulf, S., Zanchetta, G., 2014. Tephrochronology and the extended intimate (integration
723 of ice-core, marine and terrestrial records) event stratigraphy 8–128 ka b2k. Quaternary Science Reviews 106, 88-100.
724 Bourne, A.J., Albert, P.G., Matthews, I.P., Trincardi, F., Wulf, S., Asioli, A., Blockley, S.P.E., Keller, J., Lowe, J.J., 2015.
725 Tephrochronology of core PRAD 1-2 from the Adriatic Sea: insights into Italian explosive volcanism for the period 200-80 ka.
726 Quaternary Science Reviews 116, 28-43.
727 Bourne, A.J., Lowe, J.J., Trincardi, F., Asioli, A., Blockley, S.P.E., Wulf, S., Matthews, I.P., Piva, A., Vigliotti, L., 2010. Distal tephra
728 record for the last ca 105,000 years from core PRAD 1-2 in the central Adriatic Sea implications for marine tephrostratigraphy.
729 Quaternary Science Reviews 29, 3079-3094.
730 Cavinato, G.P., Carusi, C., Dall'Asta, M., Miccadei, E., Piacentini, T., 2002. Sedimentary and tectonic evolution of Plio–Pleistocene
731 alluvial and lacustrine deposits of Fucino Basin (central Italy). Sedimentary Geology 148, 29-59.
732 Channell, J. E. T., 2006, Late Brunhes polarity excursions (Mono Lake, Laschamp, Iceland Basin and Pringle Falls) recorded at ODP
733 Site 919 (Irminger Basin): Earth and Planetary Science Letters, v. 244, no. 1, p. 378-393.
734 Channell, J. E. T., 2014, The Iceland Basin excursion: Age, duration, and excursion field geometry: Geochemistry, Geophysics,
735 Geosystems, v. 15, no. 12, p. 4920-4935.
736 Cheng H, Edwards RL, Sinha A, Spötl C, Yi L, Chen S, Kelly M, Kathayat G, Wang X, Li X, Kong X, Wang Y, Ning Y, Zhang H.
737 2016. The Asian monsoon over the past 640,000 years and ice age terminations. Nature. 2016 Jun 30;534(7609):640-6. doi:
738 10.1038/nature18591.
739 De Vivo, B., Rolandi, G., Gans, P.B., Calvert, A., Bohrson, W.A., Spera, F.J., Belkin, H.E., 2001. New constraints on the pyroclastic
740 eruptive history of the Campanian volcanic Plain (Italy). Mineralogy and Petrology 73, 47-65.
741 Di Roberto, A., Smedile, A., Del Carlo, P., De Martini, P.M., Iorio, M., Petrelli, M., Pantosti, D., Pinzi, S., Todrani, A., 2018. Tephra
742 and cryptotephra in a ~ 60,000-year-old lacustrine sequence from the Fucino Basin: new insights into the major explosive
743 events in Italy. Bulletin of Volcanology 80, 20.
744 Follieri, M., Magri, D., Sadori, L., 1986. Late Pleistocene Zelkova extinction in Central Italy. New Phytologist 103, 269-273.
745 Follieri, M., Magri, D., Sadori, L., Villa, I., 1991. Palinologia e datazione radiometrica $^{40}Ar/^{39}Ar$ di un sondaggio nella piana del Fucino
746 (Abruzzo), Workshop 'Evoluzione dei bacini neogenici e loro rapporti con il magmatismo plioquaternario nell'area tosco-
747 laziale', Pisa, Italy, 12.-13. Giugno, pp. 90-92.
748 Freda, C., Gaeta, M., Karner, D.B., Marra, F., Renne, P.R., Taddeucci, J., Scarlato, P., Christensen, J.N., Dallai, L., 2006. Eruptive
749 history and petrologic evolution of the Albano multiple maar (Alban Hills, Central Italy). Bulletin of Volcanology 68, 567-
750 591.
751 Galadini, F., Galli, P., 2000. Active Tectonics in the Central Apennines (Italy) – Input Data for Seismic Hazard Assessment. Natural
752 Hazards 22, 225-268.
753 Galadini, F., Messina, P., Giaccio, B., Sposato, A., 2003. Early uplift history of the Abruzzi Apennines (central Italy): available
754 geomorphological constraints. Quaternary International 101, 125-135.
755 Galli, P., Giaccio, B., Messina, P., Peronace, E., 2016. Three magnitude 7 earthquakes on a single fault in central Italy in 1400 years,
756 evidenced by new palaeoseismic results. Terra Nova 28, 146-154.
757 Galli, P., Giaccio, B., Messina, P., Peronace, E., Amato, V., Naso, G., Nomade, S., Pereira, A., Piscitelli, S., Bellanova, J., Billi, A.,
758 Blamart, D., Galderisi, A., Giocoli, A., Stabile, T., Thil, F., 2017. Middle to Late Pleistocene activity of the northern Matese
759 fault system (southern Apennines, Italy). Tectonophysics 699, 61-81.
760 Gatta, M., Giaccio, B., Marra, F., Rolfo, M.F., Jicha, B.R., 2017. Trace-element fingerprinting of the 69–36 ka Colli Albani eruptive
761 units: A preliminary dataset for archaeological and tephra studies in central-southern Italy. Journal of Archaeological Science:
762 Reports 16, 330-340.
763 Giaccio, B., Arienzo, I., Sottili, G., Castorina, F., Gaeta, M., Nomade, S., Galli, P., Messina, P., 2013a. Isotopic (Sr-Nd) and major
764 element fingerprinting of distal tephras: an application to the Middle-Late Pleistocene markers from the Colli Albani volcano,
765 central Italy. Quaternary Science Reviews 67, 190-206.
766 Giaccio, B., Castorina, F., Nomade, S., Scardia, G., Voltaggio, M., Sagnotti, L., 2013b. Revised Chronology of the Sulmona Lacustrine
767 Succession, Central Italy. Journal of Quaternary Science 28, 545-551.

768 Giaccio, B., Galli, P., Messina, P., Peronace, E., Scardia, G., Sottili, G., Sposato, A., Chiarini, E., Jicha, B., Silvestri, S., 2012a. Fault
769 and basin depocentre migration over the last 2 Ma in the L'Aquila 2009 earthquake region, central Italian Apennines.
770 Quaternary Science Reviews 56, 69-88.
771 Giaccio, B., Galli, P., Peronace, E., Arienzo I., Nomade, S., Cavinato, G.P., Mancini, M., Messina, P., Sottili, G., 2014. A 560-440 ka
772 tephra record from the Mercure Basin, Southern Italy: volcanological and tephrostratigraphic implications. Journal of
773 Quaternary Science 29, 232-248.
774 Giaccio, B., Hajdas, I., Isaia, R., Deino, A., Nomade, S., 2017a. High-precision 14C and 40Ar/39Ar dating of the Campanian Ignimbrite
775 (Y-5) reconciles the time-scales of climatic-cultural processes at 40 ka. Scientific Reports 7, 45940.
776 Giaccio, B., Marra, F., Hajdas, I., Karner, D.B., Renne, P.R., Sposato, A., 2009. 40Ar/39Ar and 14C geochronology of the Albano
777 maar deposits: Implications for defining the age and eruptive style of the most recent explosive activity at Colli Albani Volcanic
778 District, Central Italy. Journal of Volcanology and Geothermal Research 185, 203-213.
779 Giaccio, B., Niespolo, E.M., Pereira, A., Nomade, S., Renne, P.R., Albert, P.G., Arienzo, I., Regattieri, E., Wagner, B., Zanchetta, G.,
780 Gaeta, M., Galli, P., Mannella, G., Peronace, E., Sottili, G., Florindo, F., Leicher, N., Marra, F., Tomlinson, E.L., 2017. First
781 integrated tephrochronological record for the last ~190 kyr from the Fucino Quaternary lacustrine succession, central Italy.
782 Quaternary Science Reviews 158, 211-234.
783 Giaccio, B., Nomade, S., Wulf, S., Isaia, R., Sottili, G., Cavuoto, G., Galli, P., Messina, P., Sposato, A., Sulpizio, R., Zanchetta, G.,
784 2012b. The late MIS 5 Mediterranean tephra markers: a reappraisal from peninsular Italy terrestrial records. Quaternary Science
785 Reviews 56, 31-45.
786 Giaccio, B., Regattieri, E., Zanchetta, G., Nomade, S., Renne, P.R., Sprain, C.J., Drysdale, R.N., Tzedakis, P.C., Messina, P., Scardia,
787 G., Sposato, A., Bassinot, F., 2015a. Duration and dynamics of the best orbital analogue to the present interglacial. Geology
788 43, 603-606.
789 Giaccio, B., Regattieri, E., Zanchetta, G., Wagner, B., Galli, P., Mannella, G., Niespolo, E., Peronace, E., Renne, P.R., Nomade, S.,
790 Cavinato, G.P., Messina, P., Sposato, A., Boschi, C., Florindo, F., Marra, F., Sadori, L., 2015b. A key continental archive for
791 the last 2 Ma of climatic history of the central Mediterranean region: A pilot drilling in the Fucino Basin, central Italy. Scientific
792 Drilling 20, 13-19.
793 Giaccio, B., Sposato, A., Gaeta, M., Marra, F., Palladino, D.M., Taddeucci, J., Barbieri, M., Messina, P., Rolfo, M.F., 2007. Mid-distal
794 occurrences of the Albano Maar pyroclastic deposits and their relevance for reassessing the eruptive scenarios of the most
795 recent activity at the Colli Albani Volcanic District, Central Italy. Quaternary International 171-172, 160-178.
796 Giordano, G., De Benedetti, A.A., Diana, A., Diano, G., Gaudioso, F., Marasco, F., Miceli, M., Mollo, S., Cas, R.A.F., Funiciello, R.,
797 2006. The Colli Albani mafic caldera (Roma, Italy): Stratigraphy, structure and petrology. Journal of Volcanology and
798 Geothermal Research 155, 49-80.
799 Giraudi, C., Giaccio, B., 2015. Middle Pleistocene glaciations in the Apennines, Italy: new chronological data and preservation of the
800 glacial record. Geological Society, London, Special Publications 433, 161-178.
801 Govin, A., Capron, E., Tzedakis, P.C., Verheyden, S., Ghaleb, B., Hillaire-Marcel, C., St-Onge, G., Stoner, J.S., Bassinot, F., Bazin,
802 L., Blunier, T., Combourieu-Nebout, N., El Ouahabi, A., Genty, D., Gersonde, R., Jimenez-Amat, P., Landais, A., Martrat, B.,
803 Masson-Delmotte, V., Parrenin, F., Seidenkrantz, M.S., Veres, D., Waelbroeck, C., Zahn, R., 2015. Sequence of events from
804 the onset to the demise of the Last Interglacial: Evaluating strengths and limitations of chronologies used in climatic archives.
805 Quaternary Science Reviews 129, 1-36.
806 Gouhier, T., Grinsted, A., Simko, V., 2018. biwavelet: Conduct univariate and bivariate wavelet analyses. R Package Version 02017.
807 Insinga, D.D., Tamburrino, S., Lirer, F., Vezzoli, L., Barra, M., De Lange, G.J., Tiepolo, M., Vallefuoco, M., Mazzola, S., Sprovieri,
808 M., 2014. Tephrochronology of the astronomically-tuned KC01B deep-sea core, Ionian Sea: insights into the explosive activity
809 of the Central Mediterranean area during the last 200 ka. Quaternary Science Reviews 85, 63-84.
810 Karner, D.B., Juvigne, E., Brancaccio, L., Cinque, A., Russo Ermolli, E., Santangelo, N., Bernasconi, S., Lirer, L., 1999. Apotential
811 early middle Pleistocene tephrostratotype for theMediterranean Basin: the Vallo di Diano, Campania, Italy.Global and
812 Planetary Change 21, 1–15.
813 Karner, D.B., Marra, F., Renne, P.R., 2001. The history of the Monti Sabatini and Alban Hills volcanoes: groundwork for assessing
814 volcanic-tectonic hazards for Rome. Journal of Volcanology and Geothermal Research 107, 185-219.
815 Kousis, I., Koutsodendris, A., Peyron, O., Leicher, N., Francke, A., Wagner, B., Giaccio, B., Knipping, M., Pross, J., 2018. Centennial-
816 scale vegetation dynamics and climate variability in SE Europe during Marine Isotope Stage 11 based on a pollen record from
817 Lake Ohrid. Quaternary Science Reviews 190, 20-38.
818 Lane, C.S., Lowe, D.J., Blockley, S.P.E., Suzuki, T., Smith, V.C., 2017. Advancing tephrochronology as a global dating tool:
819 Applications in volcanology, archaeology, and palaeoclimatic research. Quaternary Geochronology 40, 1-7.
820 Laurenzi, M.A., Villa, I., 1987. 40Ar/39Ar chronostratigraphy of Vico ignimbrites. Periodico di Mineralogia 56, 285-293.
821 Le Bas, M.J.L., Maitre, R.W.L., Streckeisen, A., Zanettin, B., 1986. A Chemical Classification of Volcanic Rocks Based on the Total
822 Alkali-Silica Diagram. Journal of Petrology 27, 745-750.
823 Lee, J.Y., Marti, K., Severinghaus, J.P., Kawamura, K., Yoo, H.S., Lee, J.B., Kim, J.S., 2006. A redetermination of the isotopic
824 abundances of atmospheric Ar. Geochimica Et Cosmochimica Acta 70, 4507-4512.
825 Leicher, N., Zanchetta, G., Sulpizio, R., Giaccio, B., Wagner, B., Nomade, S., Francke, A., Del Carlo, P., 2016. First tephrostratigraphic
826 results of the DEEP site record from Lake Ohrid (Macedonia and Albania). Biogeosciences 13, 2151-2178.
827 Lisiecki, L.E., Raymo, M.E., 2005. A Pliocene-Pleistocene stack of 57 globally distributed benthic δ18O records. palaeoceanography
828 20, PA1003.
829 Litt, T., Anselmetti, F.S., 2014. Lake Van deep drilling project PALAEOVAN. Quaternary Science Reviews 104, 1-7.
830 Lowe, J.J., Ramsey, C.B., Housley, R.A., Lane, C.S., Tomlinson, E.L., 2015. The RESET project: constructing a European tephra
831 lattice for refined synchronisation of environmental and archaeological events during the last c. 100 ka. Quaternary Science
832 Reviews 118, 1-17.
833 Mannella, G., Giaccio, B., Zanchetta, G., Regattieri, E., Niespolo, E.M., Pereira, A., Renne, P.R., Nomade, S., Leicher, N., Perchiazzi,
834 N., Wagner, B., 2019. Palaeoenvironmental and palaeohydrological variability of mountain areas in the central Mediterranean

region: A 190 ka-long chronicle from the independently dated Fucino palaeolake record (central Italy). Quaternary Science Reviews 210, 190-210.

Marra, F., Gaeta, M., Giaccio, B., Jicha, B.R., Palladino, D.M., Polcari, M., Sottili, G., Taddeucci, J., Florindo, F., Stramondo, S., 2016. Assessing the volcanic hazard for Rome: 40Ar/39Ar and In-SAR constraints on the most recent eruptive activity and present-day uplift at Colli Albani Volcanic District. Geophysical Research Letters 43, 6898-6906.

Marra, F., Karner, D.B., Freda, C., Gaeta, M., Renne, P., 2009. Large mafic eruptions at Alban Hills Volcanic District (Central Italy): Chronostratigraphy, petrography and eruptive behavior. Journal of Volcanology and Geothermal Research 179, 217-232.

Marra, F., Rohling, E.J., Florindo, F., Jicha, B., Nomade, S., Pereira, A., Renne., P.R., 2016. Independent $^{40}Ar/^{39}Ar$ and ^{14}C age constraints on the last five glacial terminations from the aggradational successions of the Tiber River, Rome (Italy). Earth Planet Sci Lett., 449, 105-117.

Marra, F., Sottili, G., Gaeta, M., Giaccio, B., Jicha, B., Masotta, M., Palladino, D.M., Deocampo, D.M., 2014. Major explosive activity in the Monti Sabatini Volcanic District (central Italy) over the 800-390 ka interval: geochronological-geochemical overview and tephrostratigraphic implications. Quaternary Science Reviews 94, 74-101.

Marra, F., Bahain, J.-J., Jicha, B., Nomade, S., Palladino, D.M., Pereira, A., Tolomei, C., Voinchet, P., Anzidei, M., Aureli, D., Ceruleo, P., Falguères, C., Florindo, F., Gatta, M., Ghaleb, B., La Rosa, M., Peretto, C., Petronio, C., Rocca, R., Rolfo, M.F., Salari, L., Smedile, A., Tombret, O., 2019. Reconstruction of the MIS 5.5, 5.3 and 5.1 coastal terraces in Latium (central Italy): a re-evaluation of the sea-level history in the Mediterranean Sea during the Last Interglacial. Quaternary International 525, 54–77. DOI:10.1016/j.quaint.2019.09.001.

Martrat, B., Grimalt, J.O., Shackleton, N.J., de Abreu, L., Hutterli, M.A., Stocker, T.F., 2007. Four climate cycles of recurring deep and surface water destabilizations on the Iberian margin. Science 317, 502-507.

Munno, R., Petrosino, P., 2007. The late Quaternary tephrostratigraphical record of the San Gregorio Magno basin (southern Italy). Journal of Quaternary Science 22, 247-266.

Narcisi, B., 1994. Caratteristiche e possibile provenienza di due livelli piroclastici nei sedimenti del Pleistocene superiore della piana del Fucino (Italia Centrale). Rendiconti Lincei 5, 115.

Niespolo, E.M., Rutte, D., Deino, A.L., Renne, P.R., 2017. Intercalibration and age of the Alder Creek sanidine 40Ar/ 39Ar standard. Quaternary Geochronology 39, 205-213.

Palladino, D.M., Simei, S., Sottili, G., Trigila, R., 2010. Integrated approach for the reconstruction of stratigraphy and geology of Quaternary volcanic terrains: An application to the Vulsini Volcanoes (Central Italy). Geological Society of America Special Papers 464, 63-84.

Paterne, M., Guichard, F., Duplessy, J.C., Siani, G., Sulpizio, R., Labeyrie, J., 2008. A 90,000–200,000 yrs marine tephra record of Italian volcanic activity in the Central Mediterranean Sea. Journal of Volcanology and Geothermal Research 177, 187-196.

Peccerillo, A., 2017. Cenozoic volcanism in the Tyrrhenian Sea region, in: IAVCEI (Ed.), Advances in Volcanology, 2 ed. Springer, p. 399.

Pereira, A., Nomade, S., Falguères, C., Bahain, J.-J., Tombret, O., Garcia, T., Voinchet, P., Bulgarelli, G.-M., Anzidei, A.-P., 2017. 40Ar/39Ar and ESR/U-series data for the La Polledrara di Cecanibbio archaeological site (Lazio, Italy). Journal of Archaeological Science: Reports 15, 20-29.

Pereira, A., Nomade, S., Moncel, M.H., Voinchet, P., Bahain, J.J., Biddittu, I., Falgueres, C., Giaccio, B., Manzi, G., Parenti, F., Scardia, G., Scao, V., Sottili, G., Vietti, A., 2018. Integrated geochronology of Acheulian sites from the southern Latium (central Italy): Insights on human-environment interaction and the technological innovations during the MIS 11-MIS 10 period. Quaternary Science Reviews 187, 112-129.

Perini, G., Francalanci, L., Davidson, J.P., Conticelli, S., 2004. Evolution and genesis of magmas from Vico Volcano, Central Italy: multiple differentiation pathways and variable parental magmas. Journal of Petrology 45, 139-182.

Petrosino, P., Ermolli, E.R., Donato, P., Jicha, B., Robustelli, G., Sardella, R., 2014a. Using Tephrochronology and palynology to date the MIS 13 lacustrine sediments of the Mercure Basin (Southern Apennines – Italy). Italian Journal of Geosciences 133, 169-186.

Petrosino, P., Jicha, B.R., Mazzeo, F.C., Russo Ermolli, E., 2014b. A high resolution tephrochronological record of MIS 14–12 in the Southern Apennines (Acerno Basin, Italy). Journal of Volcanology and Geothermal Research 274, 34-50.

Petrosino, P., Morabito, S., Jicha, B.R., Milia, A., Sprovieri, M., Tamburrino, S., 2016. Multidisciplinary tephrochronological correlation of marker events in the eastern Tyrrhenian Sea between 48 and 105ka. Journal of Volcanology and Geothermal Research 315, 79-99.

Railsback, L.B., Gibbard, P.L., Head, M.J., Voarintsoa, N.R.G., Toucanne, S., 2015. An optimized scheme of lettered marine isotope substages for the last 1.0 million years, and the climatostratigraphic nature of isotope stages and substages. Quaternary Science Reviews 111, 94-106.

R Core Team, 2017. R: A Language and Environment for Statistical Computing.

Regattieri, E., Giaccio, B., Galli, P., Nomade, S., Peronace, E., Messina, P., Sposato, A., Boschi, C., Gemelli, M., 2016. A multi-proxy record of MIS 11–12 deglaciation and glacial MIS 12 instability from the Sulmona basin (central Italy). Quaternary Science Reviews 132, 129-145.

Regattieri, E., Giaccio, B., Mannella, G., Zanchetta, G., Nomade, S., Tognarelli, A., Perchiazzi, N., Vogel, H., Boschi, C., Drysdale, R.N., Wagner, B., Gemelli, M., Tzedakis, P., 2019. Frequency and dynamics of millennial-scale variability during Marine Isotope Stage 19: Insights from the Sulmona Basin (central Italy). Quaternary Science Reviews 214, 28-43.

Regattieri, E., Giaccio, B., Zanchetta, G., Drysdale, R.N., Galli, P., Nomade, S., Peronace, E., Wulf, S., 2015. Hydrological variability over the Apennines during the Early Last Glacial precession minimum, as revealed by a stable isotope record from Sulmona basin, Central Italy. Journal of Quaternary Science 30, 19-31.

Renne, P.R., Balco, G., Ludwig, K.R., Mundil, R., Min, K., 2011. Response to the comment by WH Schwarz et al. on "Joint determination of 40 K decay constants and 40 Ar∗/40 K for the Fish Canyon sanidine standard, and improved accuracy for 40 Ar/39 Ar geochronology" by PR Renne et al.(2010). Geochimica et Cosmochimica Acta 75, 5097-5100.

Rodrigues, T., Alonso-Garcia, M., Hodell, D.A., Rufino, M., Naughton, F., Grimalt, J.O., Voelker, A.H.L., Abrantes, F., 2017. A 1-Ma record of sea surface temperature and extreme cooling events in the North Atlantic: A perspective from the Iberian Margin. Quaternary Science Reviews 172, 118-130.

Rodrigues, T., Voelker, A.H.L., Grimalt, J.O., Abrantes, F., Naughton, F., 2011. Iberian Margin sea surface temperature during MIS 15 to 9 (580–300 ka): Glacial suborbital variability versus interglacial stability. palaeoceanography and palaeoclimatology 26, PA1204.

Russo Ermolli, E. R., Di Donato, V., Martín-Fernández, J. A., Orain, R., Lebreton, V., & Piovesan, G., 2015. Vegetation patterns in the Southern Apennines (Italy) during MIS 13: deciphering pollen variability along a NW-SE transect. Review of Palaeobotany and Palynology, 218, 167-183

Sbrana, A., Toccaceli, R.M., 2011. Geological Map of "Isola di Ischia", 1: 10000 Scale, Foglio 464. Regione Campania-Assessorato difesa del suolo, Firenze.

Scholz, D., Hoffmann, D.L., 2011. StalAge – An algorithm designed for construction of speleothem age models. Quaternary Geochronology 6, 369-382.

Singer, B. S., Guillou, H., Jicha, B. R., Zanella, E., and Camps, P., 2014, Refining the Quaternary Geomagnetic Instability Time Scale (GITS): Lava flow recordings of the Blake and Post-Blake excursions: Quaternary Geochronology, v. 21, p. 16-28.

Smith, V.C., Isaia, R., Pearce, N.J.G., 2011. Tephrostratigraphy and glass compositions of post-15 kyr Campi Flegrei eruptions: implications for eruption history and chronostratigraphic markers. Quaternary Science Reviews 30, 3638-3660.

Sottili, G., Palladino, D.M., Marra, F., Jicha, B., Karner, D.B., Renne, P., 2010. Geochronology of the most recent activity in the Sabatini Volcanic District, Roman Province, central Italy. Journal of Volcanology and Geothermal Research 196, 20-30.

Sottili, G., Palladino, D.M., Zanon, V., 2004. Plinian activity during the early eruptive history of the Sabatini volcanic district, central Italy. Journal of Volcanology and Geothermal Research 135, 361-379.

Sulpizio, R., Zanchetta, G., D'Orazio, M., Vogel, H., Wagner, B., 2010. Tephrostratigraphy and tephrochronology of Lakes Ohrid and Prespa, Balkans. Biogeosciences 7, 3273-3288.

Tamburrino, S., Insinga, D.D., Sprovieri, M., Petrosino, P., Tiepolo, M., 2012. Major and trace element characterization of tephra layers offshore Pantelleria Island: insights into the last 200 ka of volcanic activity and contribution to the Mediterranean tephrochronology. Journal of Quaternary Science 27, 129-140.

Tauxe, L., 1993. Sedimentary records of relative paleointensity of the geomagnetic field: Theory and practice. Reviews of Geophysics, 31(3), 319-354.

Tomlinson, E.L., Albert, P.G., Wulf, S., Brown, R.J., Smith, V.C., Keller, J., Orsi, G., Bourne, A.J., Menzies, M.A., 2014. Age and geochemistry of tephra layers from Ischia, Italy: constraints from proximal-distal correlations with Lago Grande di Monticchio. Journal of Volcanology and Geothermal Research 287, 22-39.

Vakhrameeva, P., Koutsodendris, A., Wulf, S., Fletcher, W.J., Appelt, O., Knipping, M., Gertisser, R., Trieloff, M., Pross, J., 2018. The cryptotephra record of the Marine Isotope Stage 12 to 10 interval (460–335 ka) at Tenaghi Philippon, Greece: Exploring chronological markers for the Middle Pleistocene of the Mediterranean region. Quaternary Science Reviews 200, 313-333.

Vakhrameeva, P., Wulf, S., Koutsodendris, A., Tjallingii, R., Fletcher, W.J., Appelt, O., Ludwig, T., Knipping, M., Trieloff, M., Pross, J., 2019. Eastern Mediterranean volcanism during marine isotope stages 9 to 7e (335–235 ka): Insights based on cryptotephra layers at Tenaghi Philippon, Greece. Journal of Volcanology and Geothermal Research 380, 31-47.

Vazquez, J. A., and Lidzbarski, M. I., 2012, High-resolution tephrochronology of the Wilson Creek Formation (Mono Lake, California) and Laschamp event using 238U-230Th SIMS dating of accessory mineral rims: Earth and Planetary Science Letters, v. 357-358, p. 54-67.

Wastegård, S., Veres, D., Kliem, P., Hahn, A., Ohlendorf, C., Zolitschka, B., Team, T.P.S., 2013. Towards a late Quaternary tephrochronological framework for the southernmost part of South America–the Laguna Potrok Aike tephra record. Quaternary Science Reviews 71, 81-90.

Wulf, S., Keller, J., Paterne, M., Mingram, J., Lauterbach, S., Opitz, S., Sottili, G., Giaccio, B., Albert, P.G., Satow, C., Tomlinson, E.L., Viccaro, M., Brauer, A., 2012. The 100–133 ka record of Italian explosive volcanism and revised tephrochronology of Lago Grande di Monticchio. Quaternary Science Reviews 58, 104-123.

Wulf, S., Kraml, M., Brauer, A., Keller, J., Negendank, J.F.W., 2004. Tephrochronology of the 100ka lacustrine sediment record of Lago Grande di Monticchio (Southern Italy). Quaternary International 122, 7-30.

Zanchetta, G., Giaccio, B., Bini, M., Sarti, L., 2018. Tephrostratigraphy of Grotta del Cavallo, Southern Italy: Insights on the chronology of Middle to Upper Palaeolithic transition in the Mediterranean. Quaternary Science Reviews 182, 65-77.

Zanchetta, G., Sulpizio, R., Giaccio, B., Siani, G., Paterne, M., Wulf, S., D'Orazio, M., 2008. The Y-3 tephra: A Last Glacial stratigraphic marker for the Central Mediterranean Basin. Journal of Volcanology and Geothermal Research 177, 145-154.

Figure and Table captions

Table 1. Analysed tephra layers from core F4-F5.

Figure 1. Reference map of the Fucino Basin. (**a**) Location of Fucino Basin with respect to the main Quaternary Italian volcanic centres. (b) Shaded relief map showing the location of the GL, TS, SP, F1-F3 (Giaccio et al., 2015b; 2017a), F4-F5 (Mannella et al., 2019, this study), FUC-S5-6 (Di Roberto et al., 2018) boreholes in the Fucino Basin. See legend in inset for the meaning of symbols. (c) Seismic Line 1 (see trace in panel b) showing the internal architecture of the Plio-Quaternary continental deposits of the Fucino Basin along a W-E oriented

964 profile (Cavinato et al., 2002). The projected location of various boreholes on Line 1 is also shown. Seismic
965 facies interpretation of the sedimentary infill is according to Cavinato et al. (2002).
966
967 **Figure 2**. Example of correlation between the overlapped F4 and F5 core sections and of the selection of the
968 intervals used for building the composite F4-F5 record. Note that the gaps in-between two consecutive
969 individual core sections of F4 borehole are documented in F5 borehole, and vice versa.
970
971 **Figure 3**. Tephrostratigraphy, selected proxy data and general chronological framework for the newly F4-F5
972 and the previously investigated F1-F3 (Giaccio et al., 2017; Mannella et al., 2019). **(a)** Magnetic susceptibility
973 from Fucino F4 downhole logging (black) and its logarithmic representation (green) to show similarity to
974 gamma ray and Ca data. **(b)** Gamma ray from Fucino F4 downhole logging. **(c)** Selected tephra from core F4-
975 F5 investigated in this study. **(d)** Inclination data after the 16 mT AF step with tentative position of the
976 Laschamp (LE) Blake and Iceland Basin (IBE) geomagnetic excursions. **(e)** Complete tephra record and Ca
977 counts from XRF scanning in core F4-F5. Five stratigraphic intervals with relatively high Ca counts are
978 highlighted in yellow and correlated to the warm Marine Isotope Stage (MIS) 1 to 11 (the threshold is at 22700
979 cps, see text for explanation). **(f)** Complete tephra record and Ca counts from XRF scanning in core F1-F3
980 (Giaccio et al., 2017; Mannella et al., 2019). **(g)** Combined tephrochronology of F1-F3 and F4-F5 core. **(h)**
981 LR04 stack of marine benthic oxygen isotope records (Lisiecki and Raymo, 2005). Data source: $^{40}Ar/^{39}Ar$, ^{14}C,
982 astrochronological, modelled ages and correlation of tephra of the last 190 kyr: Giaccio et al. (2017) and
983 Mannella et al. (2019) and reference therein. The boundaries of the marine isotope stages (MIS) are according
984 to Railsback et al. (2015).
985
986 **Figure 4**. Representative major element compositions for the analysed F4-F5 tephra layers. (**a**) Total alkali
987 versus silica classification diagram (Le Bas et al., 1986) of the F4-F5 tephra distinguished in two compositional
988 groups (CG1 and CG2). (**b**) CaO/FeO vs Cl discriminating diagram of the volcanic sources of the Italian
989 potassic trachyte-phonolite and tephriphonolite tephra (modified from Giaccio et al., 2017) for the F4-F5
990 tephra. The CaO/FeO vs Cl diagram has been updated with the following data: Roccamonfina: Amato et al.
991 (2014) and Galli et al. (2017); Vulsini, Vico Period I (P-I) and Period II (P-II) and Sabatini: this study and
992 Author's unpublished data. For other references, the readers are referred to Giaccio et al. (2017).
993
994 **Figure 5**. Age probability density spectra diagram (left) and inverse isochrone (right) of tephra TF-126
995 (sampling code; F5-58 64-66). Blue and white bars/ indicate the individual ages included and discarded as
996 weighted mean age, respectively.
997
998 **Figure 6**. Total alkali versus silica classification diagram after Le Bas et al. (1986)and representative bi-plots
999 for the tephra F5-8 77-92 **(a)**, F5-8 148-155 **(b)** and F8-12 89-91 **(c)** from theF4-F5 record compared with their
1000 equivalents in core F1-F3. Data source: glass-WDS of Fucino TF-4, TF-5 and TF-8: Giaccio et al. (2017);
1001 $^{40}Ar/^{39}Ar$ age of Fucino TF-5: weighted mean of dating from (Freda et al., 2006; Giaccio et al., 2009; Giaccio
1002 et al., 2017), and Mannella et al. (2019); glass composition of Albano 7 Colli Albani: Giaccio et al. (2007);
1003 $^{40}Ar/^{39}Ar$ age of Albano 7 and Albano 3: weighted mean of dating from Freda et al. (2006) and Giaccio et al.
1004 (2007). $^{40}Ar/^{39}Ar$ ages are recalculated relative to an age of 1.1891 Ma for the Alder Creek sanidine monitor
1005 standard (Niespolo et al., 2017), with the uncertainty expressed at 2σ.
1006
1007 **Figure 7**. Total alkali versus silica classification diagram Le Bas et al. (1986) and representative bi-plots for
1008 the tephra F5-8 148-149 **(a)**, F5-15 90-91 **(b),** F5-20 89-91 **(c)** from core F4-F5 compared with their equivalents
1009 in core F1-F3 and with some selected proximal or distal counterparts. For comparison, in panel **(b)** also the
1010 composition of X-6 layer (grey text), not correlated with F5-15 90-91, is showed. Data source: glass-WDS and
1011 $^{40}Ar/^{39}Ar$ age of Fucino TF-7: Giaccio et al. (2017); glass-WDS and $^{40}Ar/^{39}Ar$ age of Monte Epomeo Green
1012 Tuff: Tomlinson et al. (2014)) and Sbrana and Toccaceli (2011), respectively; glass-WDS of PRAD-1870:
1013 Bourne et al. (2010); glass-WDS TF-12 and TF-13 Giaccio et al. (2017); glass-WDS and $^{40}Ar/^{39}Ar$ age of
1014 Sulmona POP3 and POP4 tephra layers: Giaccio et al. (2012b) and Regattieri et al. (2015), respectively; glass-
1015 EDS glass-WDS and $^{40}Ar/^{39}Ar$ age of TF-17: Giaccio et al. (2017); glass-EDS and $^{40}Ar/^{39}Ar$ age of CET1-18:
1016 Petrosino et al. (2016); glass-EDS and $^{40}Ar/^{39}Ar$ age of the proximal Taurano Ignimbrite: Amato et al. (2018)

and De Vivo et al. (2001), respectively; glass-EDS and $^{40}Ar/^{39}Ar$ age of S11 PAUP: Amato et al. (2018). The tephra age reported on top of each figure panel is the weighted mean of the $^{40}Ar/^{39}Ar$ ages indicated in the respective panel. $^{40}Ar/^{39}Ar$ ages are recalculated relatively to an age of 1.1891 Ma for the Alder Creek sanidine monitor standard (Niespolo et al., 2017), with the uncertainty expressed at 2σ.

Figure 8. Total alkali versus silica classification diagram after Le Bas et al. (1986) and representative bi-plots for the tephra TF-85 **(a)**, TF-117 **(b)**, and TF-118 **(c)** from the F4-F5 record compared with their proximal or distal counterparts. Data source: glass-WDS and $^{40}Ar/^{39}Ar$ age of Villa Senni proximal units: (Marra et al., 2009, 2019); glass-WDS and $^{40}Ar/^{39}Ar$ age of Villa Senni distal (PAG-t4): (Giaccio et al., 2012a); glass-WDS and $^{40}Ar/^{39}Ar$ age Pozzolane Nere fallout: (glass-WDS): (Marra et al., 2009); glass-WDS and $^{40}Ar/^{39}Ar$ age Fontana Ranuccio 2 (glass-WDS): (Pereira et al., 2018). The tephra age reported on top of each figure panel is the weighted mean of the $^{40}Ar/^{39}Ar$ ages indicated in the respective panel. $^{40}Ar/^{39}Ar$ ages are recalculated relatively to an age of 1.1891 Ma for the Alder Creek sanidine monitor standard (Niespolo et al., 2017), with the uncertainty expressed at 2σ.

Figure 9. Total alkali versus silica classification diagram after Le Bas et al. (1986) and representative bi-plots for the tephra TF-62 **(a)** and TF-126 **(b)** of the F4-F5 succession compared with their proximal counterparts. TF-126 is also compared with some geochronologically compatible but geochemically different tephra R99-30C (Tiber River successions), OH-DP 1733 (Lake Ohrid) and MOL 13 (Bojano Basin). Data source: glass-WDS of Tufo Giallo di Sacrofano and Castel Broco: this study; $^{40}Ar/^{39}Ar$ age of Tufo Giallo di Sacrofano: Sottili et al. (2010); glass-WDS and $^{40}Ar/^{39}Ar$ age of R94-30C: this study and Marra et al. (2016) respectively; glass-WDS of OH-DP 1733: Leicher et al. (in review); glass-WDS of MOL 13: Amato et al. (2014). The tephra age reported on top of each figure panel is the weighted mean of the $^{40}Ar/^{39}Ar$ ages indicated in the respective panel. $^{40}Ar/^{39}Ar$ ages are recalculated relatively to an age of 1.1891 Ma for the Alder Creek sanidine monitor standard (Niespolo et al., 2017), with the uncertainty expressed at 2σ.

Figure 10. Detailed proxy and tephra correlation of the F1-F3 record with the corresponding interval in core F4-F5. The two tephra records are merged for a composite F1-F3/F4-F5 tephra record. Note that tephra found only in F1-F3 or F4-F5 are transferred from one to the other via climatostratigraphic positions.

Figure 11. Composite F1-F3/F4-F5 tephra record. References: [a] Mannella et al. (2019 and references therein); [b] Petrosino et al. (2016) [c] Amato et al. (2018); [d] De Vivo et al.. (2001); [e] Sottili et al. (2010); [f] Marra et al. (2009); [g] Marra et al. (2019); [h] Giaccio et al. (2012); [i] Pereira et al. (2018); [j] This study. $^{40}Ar/^{39}Ar$ ages are recalculated relatively to an age of 1.1891 Ma for the Alder Creek sanidine monitor standard (Niespolo et al., 2017), with the uncertainty expressed at 2σ.

Figure 12. Preliminary age model for the composite F1-F3/F4-F5 tephra and F4-F5 Ca and palaeomagnetic records. The Fucino calcium record is compared with the sea surface temperature (SST) record from the SW Iberian Margin core MD01-2444/43 (dark red, Martrat et al., 2007) and core U1385 (red Rodrigues et al., 2017). The boundaries of the marine isotope stages (MIS) Iberian Margin record and are projected in the Fucino record along the intercept points of the yellow/blue bars with the dashed green line, which is the linear interpolation between the mid-point of the tephra ages reported in Figure 9. The ages of Fucino tephras (dashed pink lines) are in turn projected in the time-scale of the Iberian Margin SST records, that are based on their own age models (Martrat et al., 2007; Rodrigues et al., 2011). The interceptions of the orange bars with the dashed green line also provide an age estimation for the Laschamp, Blake and Iceland Basin geomagnetic excursions, as inferred from the preliminary palaeomagnetic data.

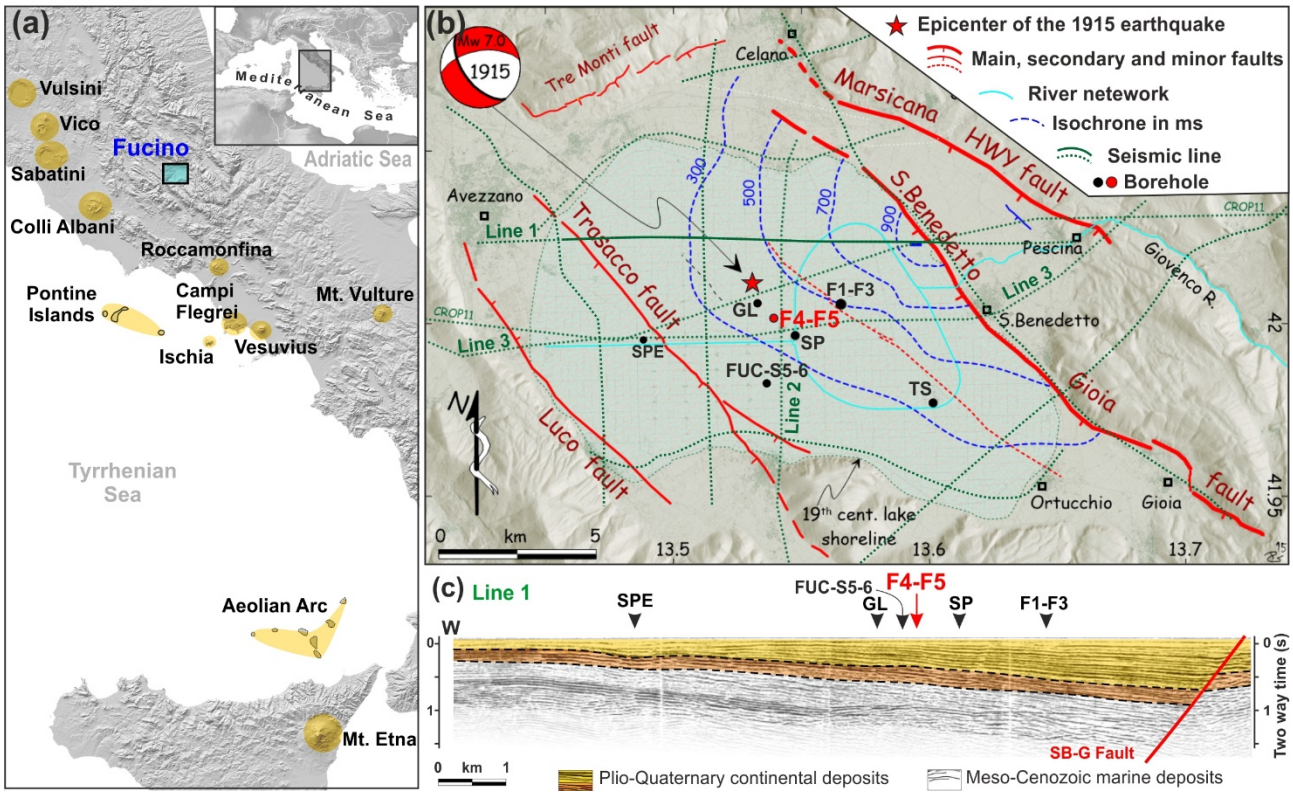

Figure 1. Reference map of the Fucino Basin. **(a)** Location of Fucino Basin with respect to the main Quaternary Italian volcanic centres. **(b)** Shaded relief map showing the location of the GL, TS, SP, F1-F3 (Giaccio et al., 2015b; 2017a), F4-F5 (Mannella et al., 2019, this study), FUC-S5-6 (Di Roberto et al., 2018) boreholes in the Fucino Basin. See legend in inset for the meaning of symbols. **(c)** Seismic Line 1 (see trace in panel b) showing the internal architecture of the Plio-Quaternary continental deposits of the Fucino Basin along a W-E oriented profile (Cavinato et al., 2002). The projected location of various boreholes on Line 1 is also shown. Seismic facies interpretation of the sedimentary infill is according to Cavinato et al. (2002).

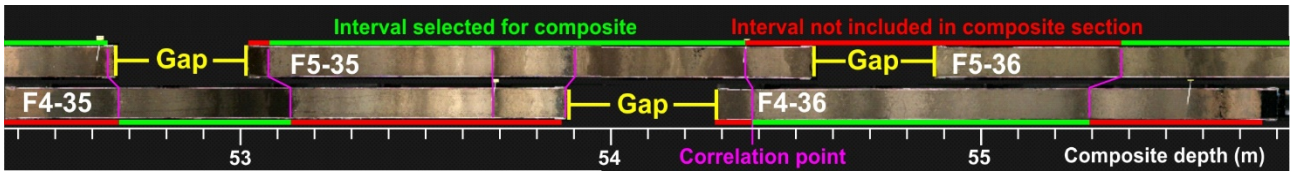

Figure 2. Example of correlation between the overlapped F4 and F5 core sections and of the selection of the intervals used for building the composite F4-F5 record. Note that the gaps in-between two consecutive individual core sections of F4 borehole are documented in F5 borehole, and vice versa.

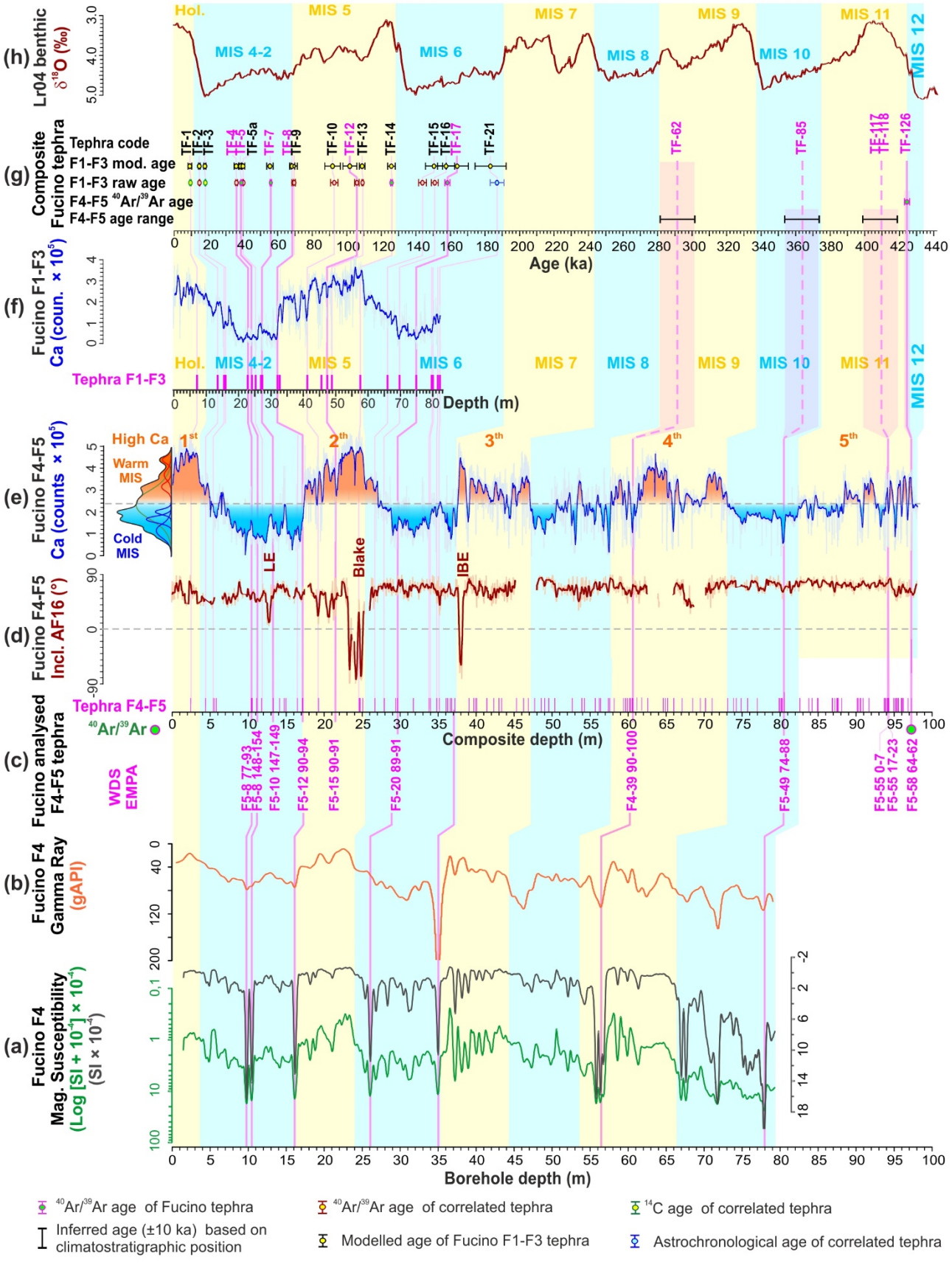

Figure 3. Tephrostratigraphy, selected proxy data and general chronological framework for the newly F4-F5 and the previously investigated F1-F3 (Giaccio et al., 2017; Mannella et al., 2019). **(a)** Magnetic susceptibility from Fucino F4 downhole logging (black) and its logarithmic representation (green) to show similarity to gamma ray and Ca data. **(b)** Gamma ray from Fucino F4 downhole logging. **(c)** Selected tephra from core F4-

F5 investigated in this study. **(d)** Inclination data after the 16 mT AF step with tentative position of the Laschamp (LE) Blake and Iceland Basin (IBE) geomagnetic excursions. **(e)** Complete tephra record and Ca counts from XRF scanning in core F4-F5. Five stratigraphic intervals with relatively high Ca counts are highlighted in yellow and correlated to the warm Marine Isotope Stage (MIS) 1 to 11 (the threshold is at 22700 cps, see text for explanation). **(f)** Complete tephra record and Ca counts from XRF scanning in core F1-F3 (Giaccio et al., 2017; Mannella et al., 2019). **(g)** Combined tephrochronology of F1-F3 and F4-F5 core. **(h)** LR04 stack of marine benthic oxygen isotope records (Lisiecki and Raymo, 2005). Data source: $^{40}Ar/^{39}Ar$, ^{14}C, astrochronological, modelled ages and correlation of tephra of the last 190 kyr: Giaccio et al. (2017) and Mannella et al. (2019) and reference therein. The boundaries of the marine isotope stages (MIS) are according to Railsback et al. (2015).

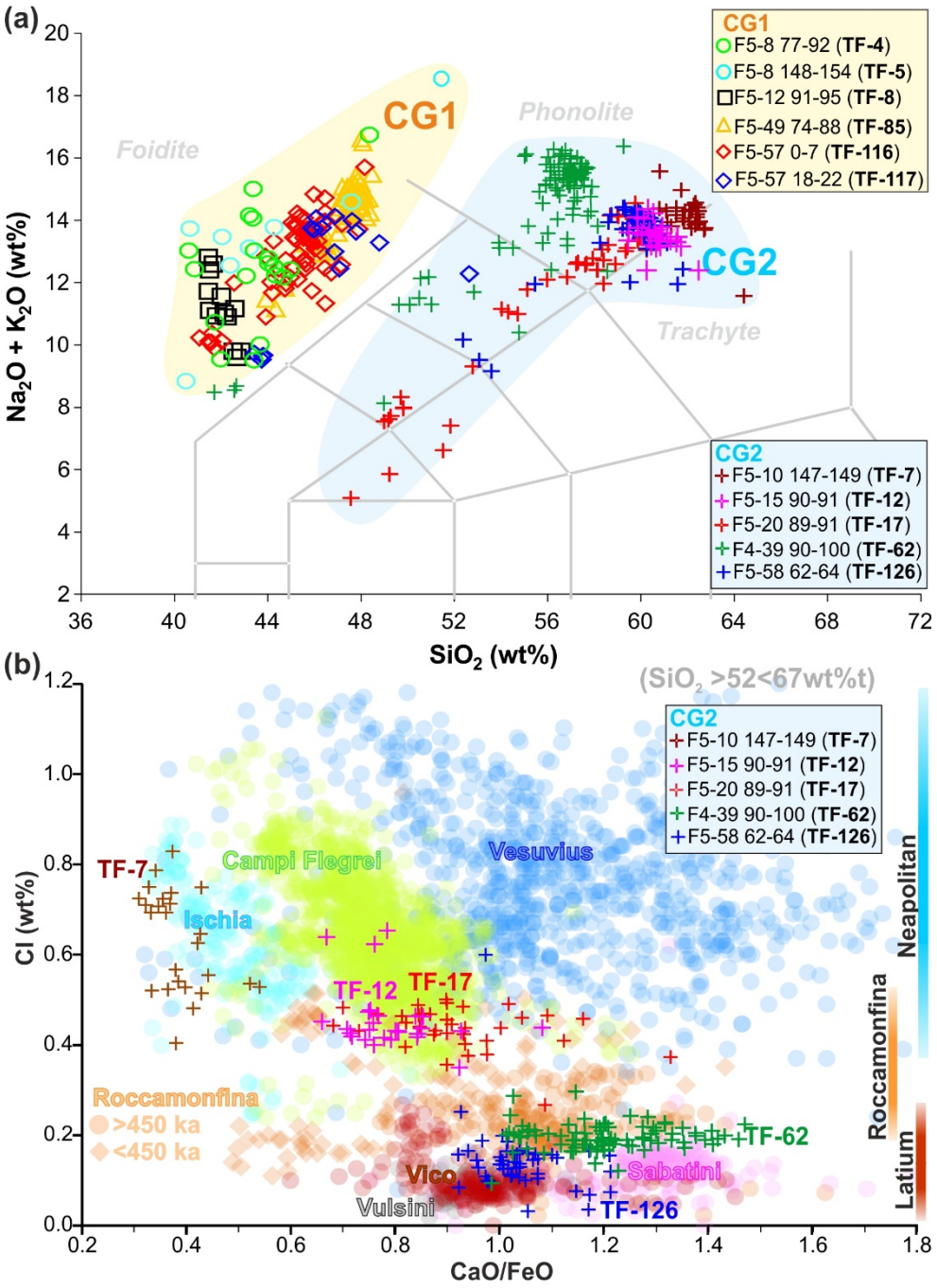

Figure 4. Representative major element compositions for the analysed F4-F5 tephra layers. (**a**) Total alkali versus silica classification diagram (Le Bas et al., 1986) of the F4-F5 tephra distinguished in two compositional groups (CG1 and CG2). (**b**) CaO/FeO vs Cl discriminating diagram of the volcanic sources of the Italian

potassic trachyte-phonolite and tephriphonolite tephra (modified from Giaccio et al., 2017) for the F4-F5 tephra. The CaO/FeO vs Cl diagram has been updated with the following data: Roccamonfina: Amato et al. (2014) and Galli et al. (2017); Vulsini, Vico Period I (P-I) and Period II (P-II) and Sabatini: this study and Author's unpublished data. For other references, the readers are referred to Giaccio et al. (2017).

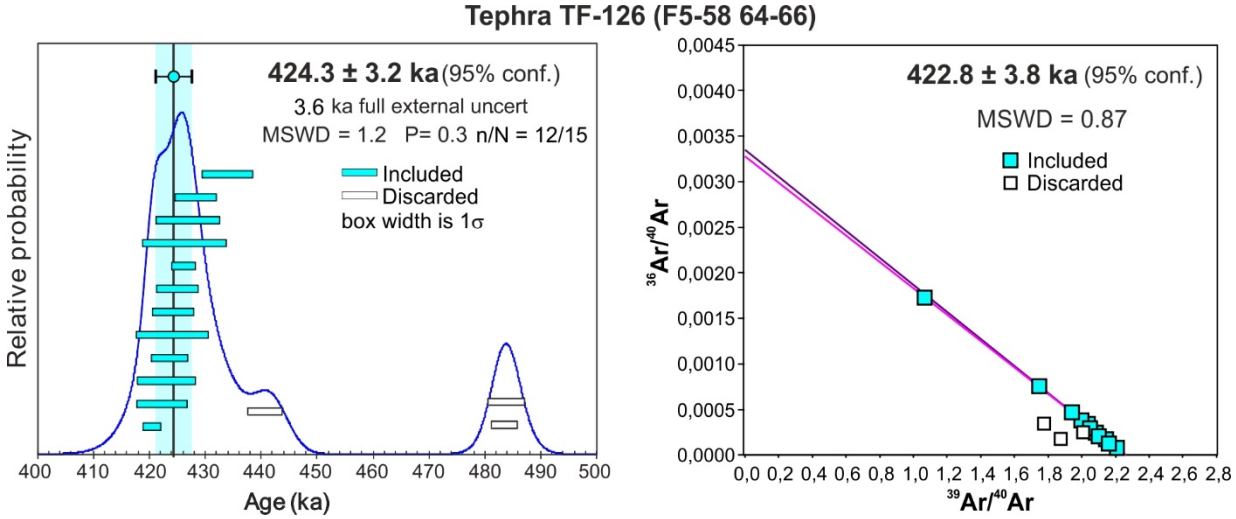

Figure 5. Age probability density spectra diagram (left) and inverse isochrone (right) of tephra TF-126 (sampling code; F5-58 64-66). Blue and white bars/ indicate the individual ages included and discarded as weighted mean age, respectively.

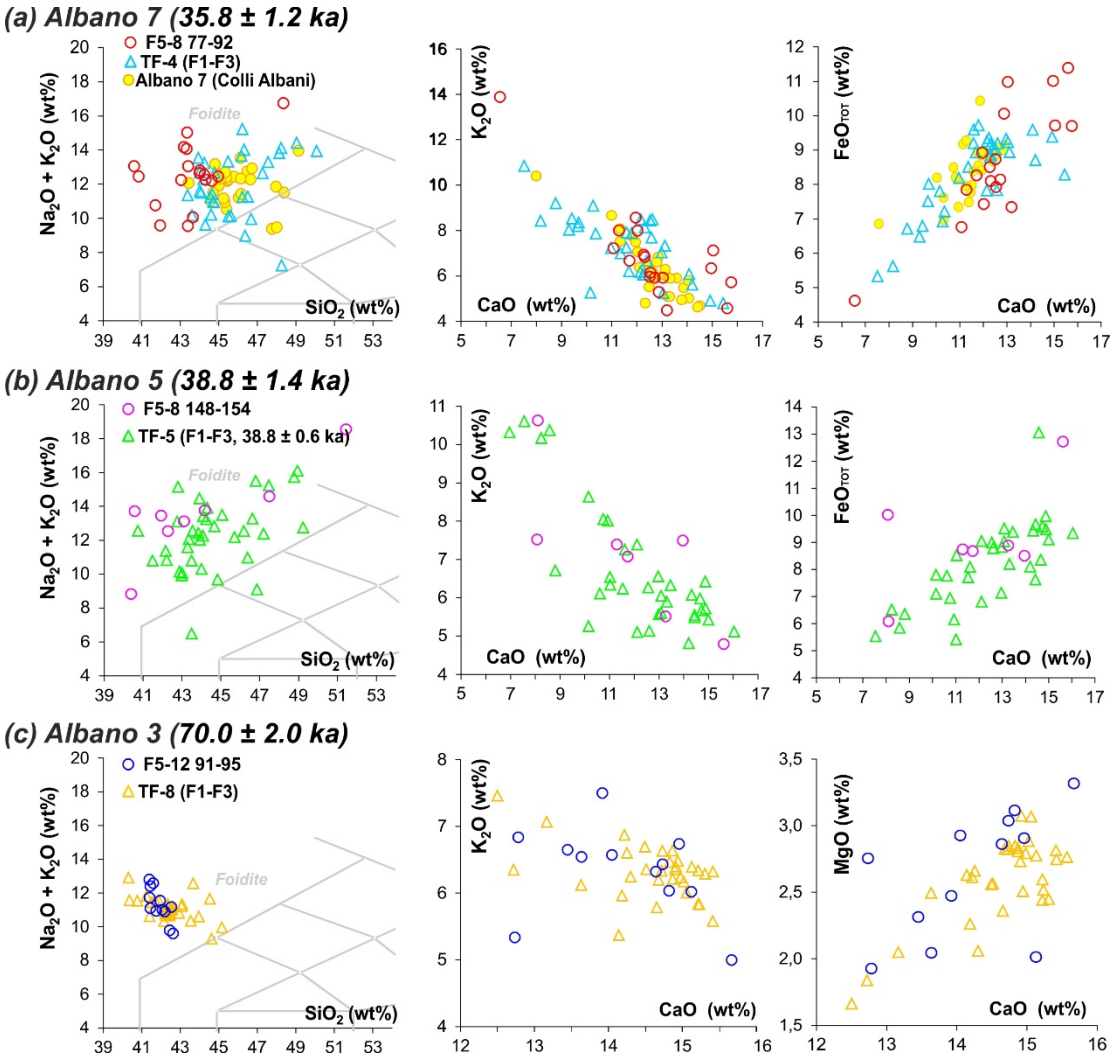

Figure 6. Total alkali versus silica classification diagram after Le Bas et al. (1986)and representative bi-plots for the tephra F5-8 77-92 **(a)**, F5-8 148-155 **(b)** and F8-12 89-91 **(c)** from theF4-F5 record compared with their equivalents in core F1-F3. Data source: glass-WDS of Fucino TF-4, TF-5 and TF-8: Giaccio et al. (2017); $^{40}Ar/^{39}Ar$ age of Fucino TF-5: weighted mean of dating from (Freda et al., 2006; Giaccio et al., 2009; Giaccio et al., 2017), and Mannella et al. (2019); glass composition of Albano 7 Colli Albani: Giaccio et al. (2007); $^{40}Ar/^{39}Ar$ age of Albano 7 and Albano 3: weighted mean of dating from Freda et al. (2006) and Giaccio et al. (2007). $^{40}Ar/^{39}Ar$ ages are recalculated relative to an age of 1.1891 Ma for the Alder Creek sanidine monitor standard (Niespolo et al., 2017), with the uncertainty expressed at 2σ.

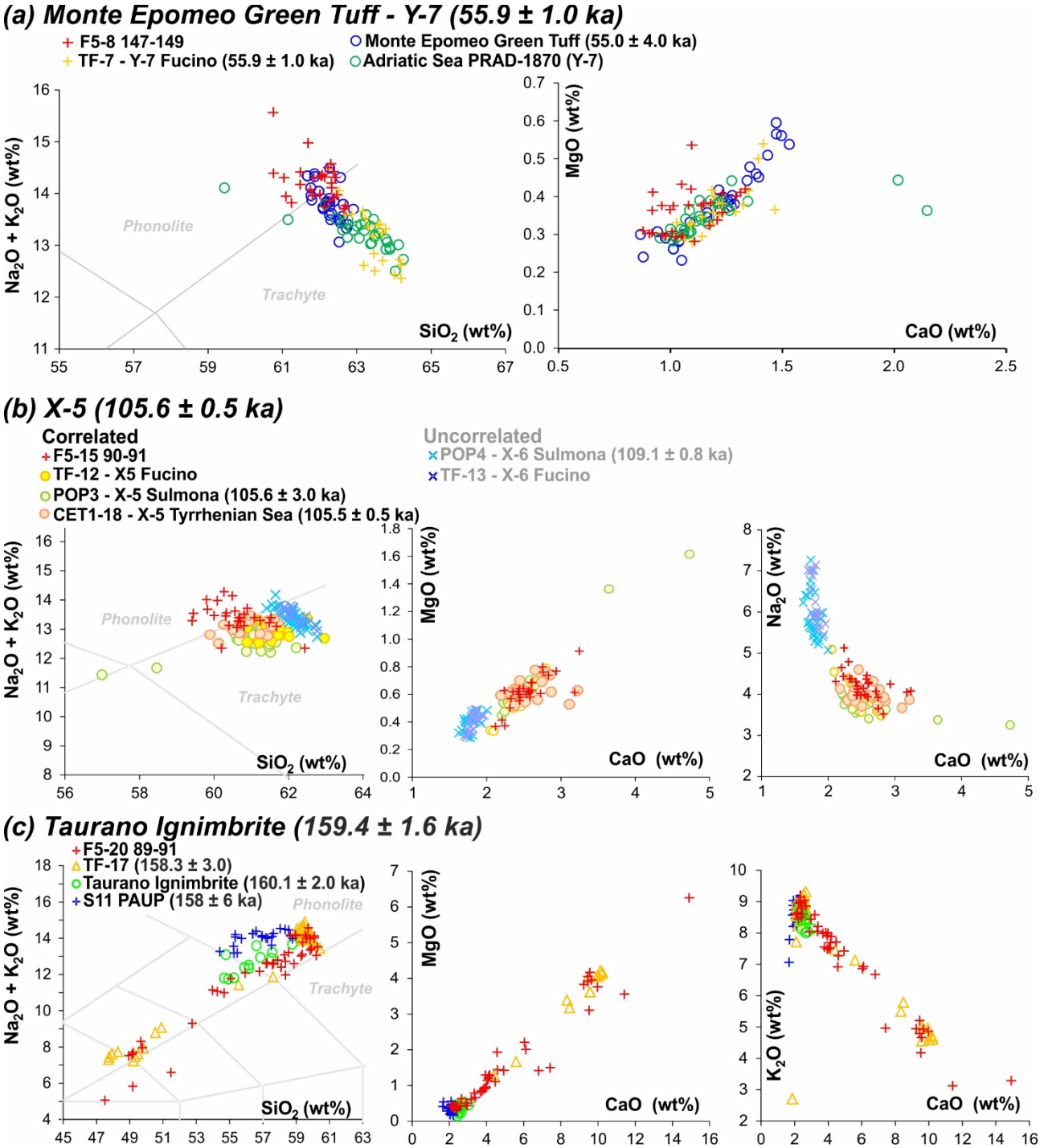

Figure 7. Total alkali versus silica classification diagram Le Bas et al. (1986) and representative bi-plots for the tephra F5-8 148-149 **(a)**, F5-15 90-91 **(b),** F5-20 89-91 **(c)** from core F4-F5 compared with their equivalents in core F1-F3 and with some selected proximal or distal counterparts. For comparison, in panel **(b)** also the composition of X-6 layer (grey text), not correlated with F5-15 90-91, is showed. Data source: glass-WDS and

$^{40}Ar/^{39}Ar$ age of Fucino TF-7: Giaccio et al. (2017); glass-WDS and $^{40}Ar/^{39}Ar$ age of Monte Epomeo Green Tuff: Tomlinson et al. (2014)) and Sbrana and Toccaceli (2011), respectively; glass-WDS of PRAD-1870: Bourne et al. (2010); glass-WDS TF-12 and TF-13 Giaccio et al. (2017); glass-WDS and $^{40}Ar/^{39}Ar$ age of Sulmona POP3 and POP4 tephra layers: Giaccio et al. (2012b) and Regattieri et al. (2015), respectively; glass-EDS glass-WDS and $^{40}Ar/^{39}Ar$ age of TF-17: Giaccio et al. (2017); glass-EDS and $^{40}Ar/^{39}Ar$ age of CET1-18: Petrosino et al. (2016); glass-EDS and $^{40}Ar/^{39}Ar$ age of the proximal Taurano Ignimbrite: Amato et al. (2018) and De Vivo et al. (2001), respectively; glass-EDS and $^{40}Ar/^{39}Ar$ age of S11 PAUP: Amato et al. (2018). The tephra age reported on top of each figure panel is the weighted mean of the $^{40}Ar/^{39}Ar$ ages indicated in the respective panel. $^{40}Ar/^{39}Ar$ ages are recalculated relatively to an age of 1.1891 Ma for the Alder Creek sanidine monitor standard (Niespolo et al., 2017), with the uncertainty expressed at 2σ.

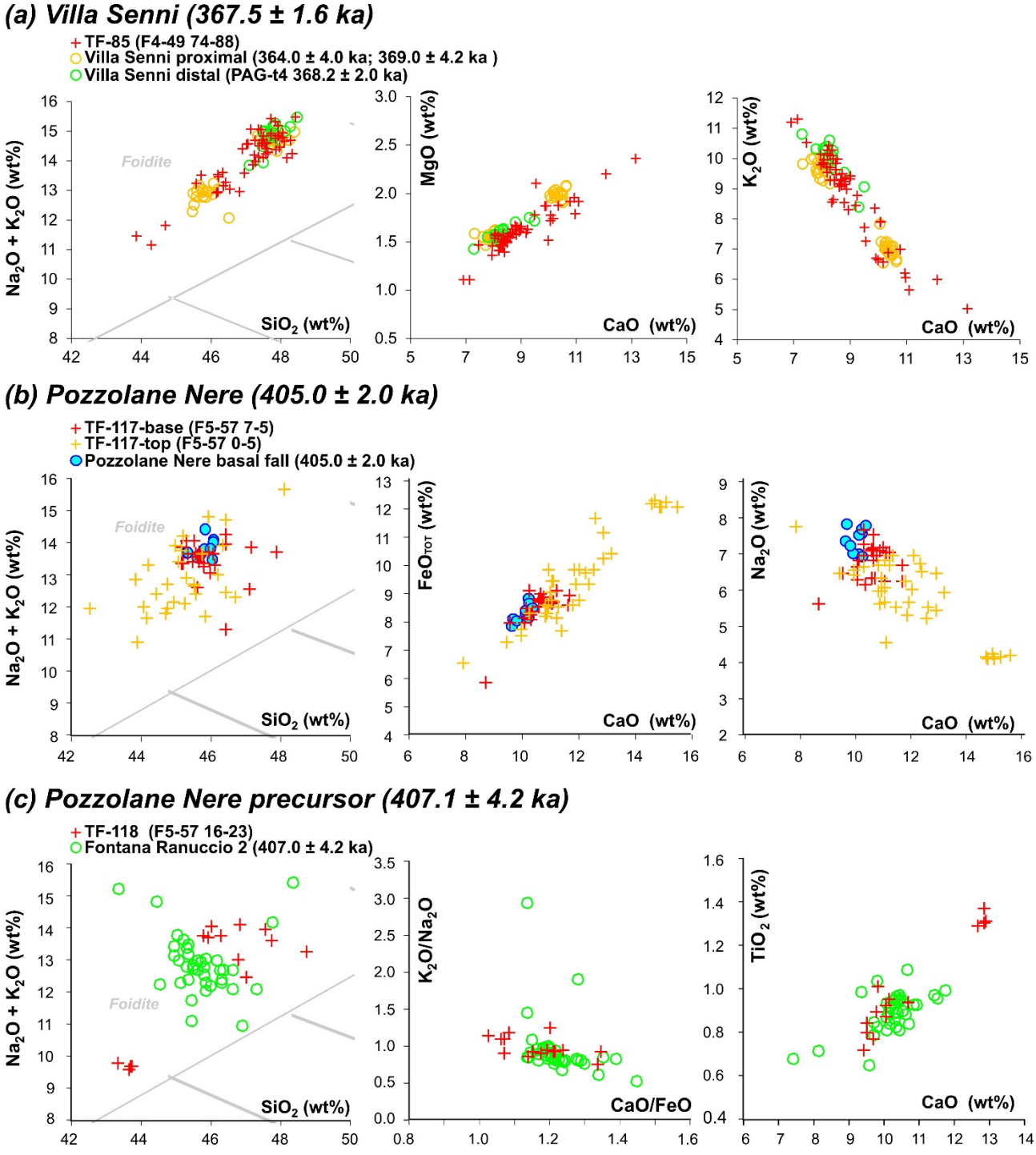

Figure 8. Total alkali versus silica classification diagram after Le Bas et al. (1986) and representative bi-plots for the tephra TF-85 **(a)**, TF-117 **(b)**, and TF-118 **(c)** from the F4-F5 record compared with their proximal or distal counterparts. Data source: glass-WDS and $^{40}Ar/^{39}Ar$ age of Villa Senni proximal units: (Marra et al., 2009, 2019); glass-WDS and $^{40}Ar/^{39}Ar$ age of Villa Senni distal (PAG-t4): (Giaccio et al., 2012a); glass-WDS and $^{40}Ar/^{39}Ar$ age Pozzolane Nere fallout: (glass-WDS): (Marra et al., 2009); glass-WDS and $^{40}Ar/^{39}Ar$ age Fontana Ranuccio 2 (glass-WDS): (Pereira et al., 2018). The tephra age reported on top of each figure panel is the weighted mean of the $^{40}Ar/^{39}Ar$ ages indicated in the respective panel. $^{40}Ar/^{39}Ar$ ages are recalculated

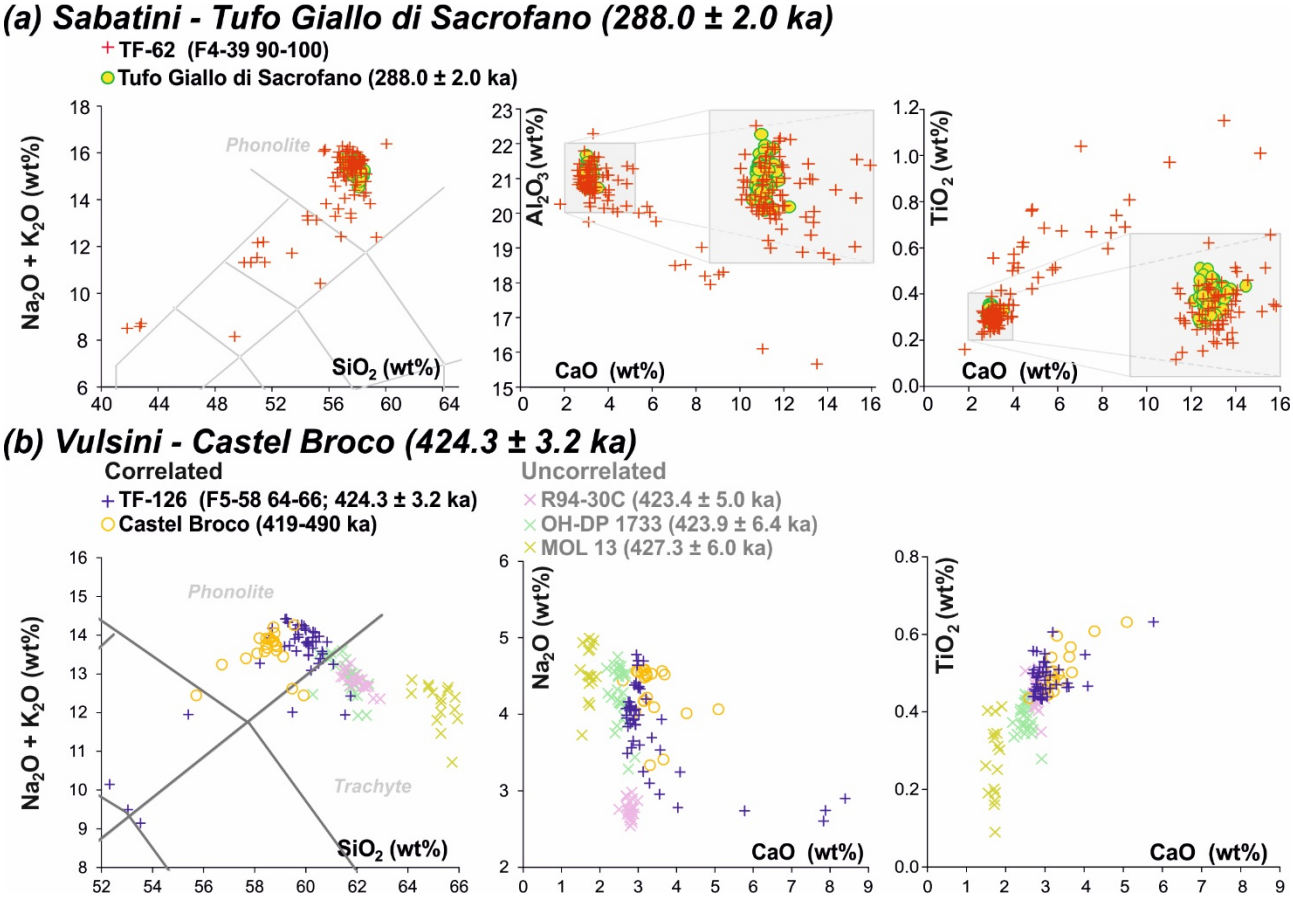

Figure 9. Total alkali versus silica classification diagram after Le Bas et al. (1986) and representative bi-plots for the tephra TF-62 **(a)** and TF-126 **(b)** of the F4-F5 succession compared with their proximal counterparts. TF-126 is also compared with some geochronologically compatible but geochemically different tephra R99-30C (Tiber River successions), OH-DP 1733 (Lake Ohrid) and MOL 13 (Bojano Basin). Data source: glass-WDS of Tufo Giallo di Sacrofano and Castel Broco: this study; $^{40}Ar/^{39}Ar$ age of Tufo Giallo di Sacrofano: Sottili et al. (2010); glass-WDS and $^{40}Ar/^{39}Ar$ age of R94-30C: this study and Marra et al. (2016) respectively; glass-WDS of OH-DP 1733: Leicher et al. (in review); glass-WDS of MOL 13: Amato et al. (2014). The tephra age reported on top of each figure panel is the weighted mean of the $^{40}Ar/^{39}Ar$ ages indicated in the respective panel. $^{40}Ar/^{39}Ar$ ages are recalculated relatively to an age of 1.1891 Ma for the Alder Creek sanidine monitor standard (Niespolo et al., 2017), with the uncertainty expressed at 2σ.

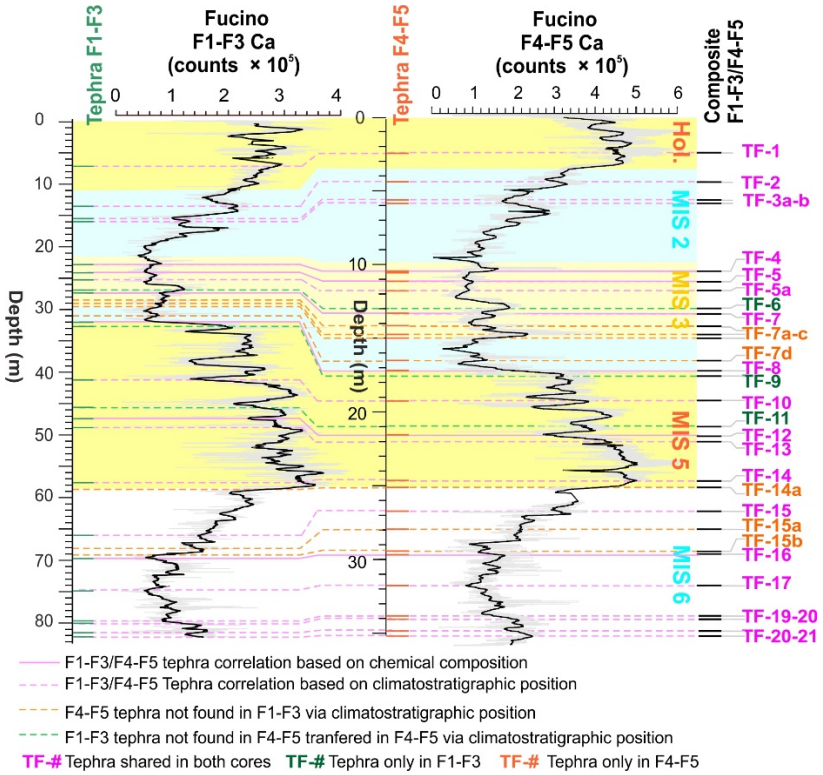

Figure 10. Detailed proxy and tephra correlation of the F1-F3 record with the corresponding interval in core F4-F5. The two tephra records are merged for a composite F1-F3/F4-F5 tephra record. Note that tephra found only in F1-F3 or F4-F5 are transferred from one to the other via climatostratigraphic positions.

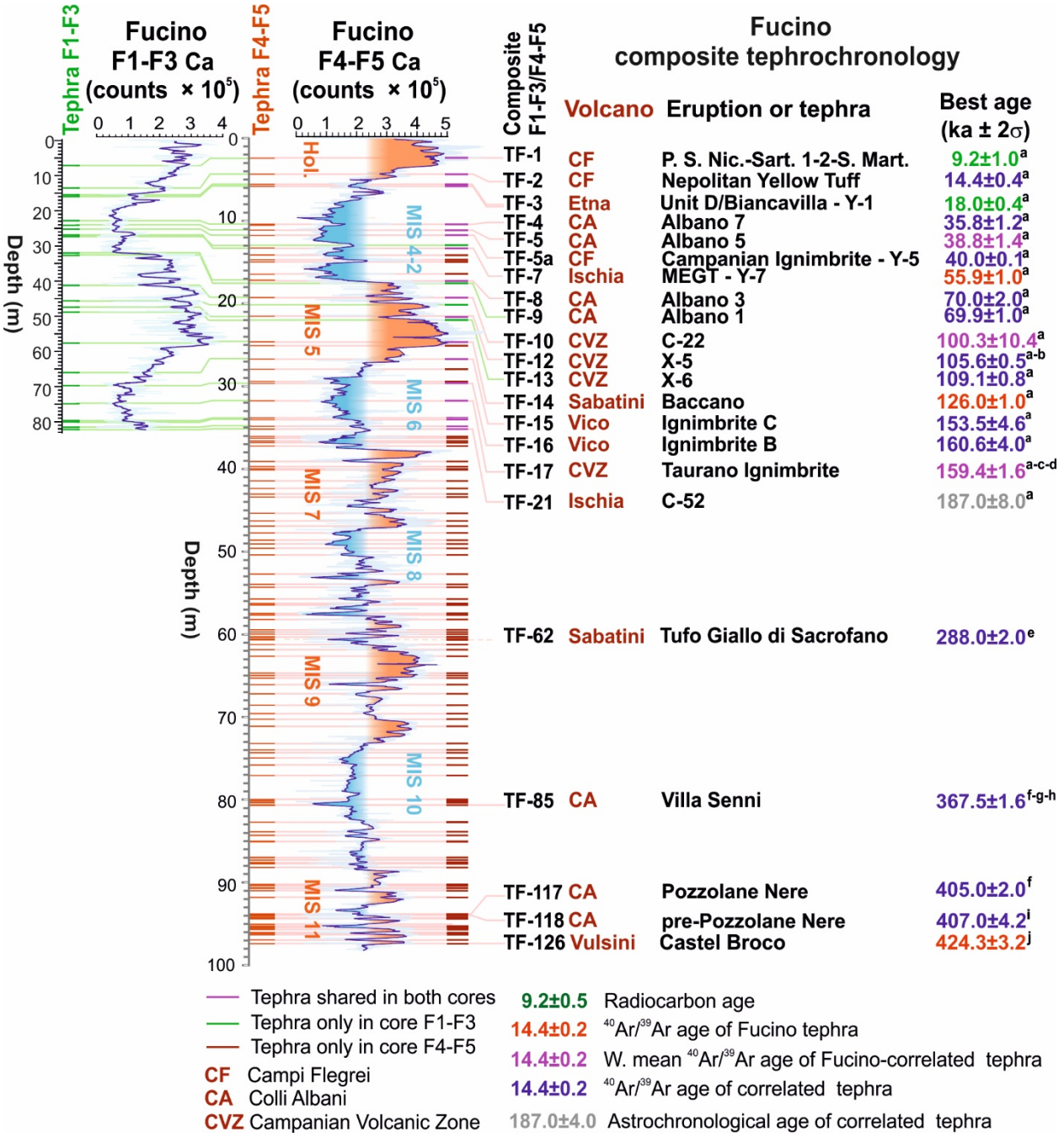

Figure 11. Composite F1-F3/F4-F5 tephra record. References: [a] Mannella et al. (2019 and references therein); [b] Petrosino et al. (2016) [c] Amato et al. (2018); [d] De Vivo et al.. (2001); [e] Sottili et al. (2010); [f] Marra et al. (2009); [g] Marra et al. (2019); [h] Giaccio et al. (2012); [i] Pereira et al. (2018); [j] This study. $^{40}Ar/^{39}Ar$ ages are recalculated relatively to an age of 1.1891 Ma for the Alder Creek sanidine monitor standard (Niespolo et al., 2017), with the uncertainty expressed at 2σ.

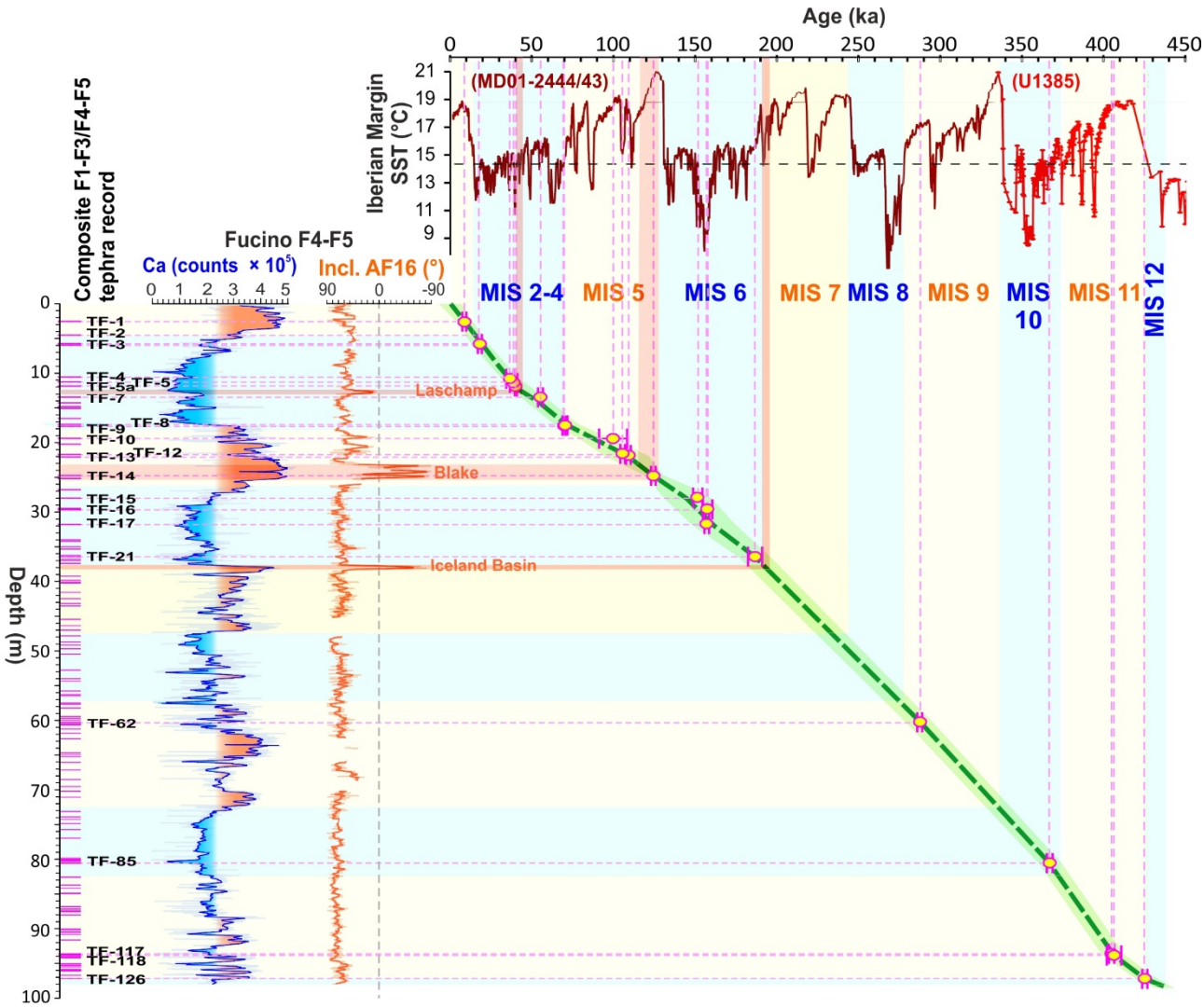

Figure 12. Preliminary age model for the composite F1-F3/F4-F5 tephra and F4-F5 Ca and palaeomagnetic records. The Fucino calcium record is compared with the sea surface temperature (SST) record from the SW Iberian Margin core MD01-2444/43 (dark red, Martrat et al., 2007) and core U1385 (red Rodrigues et al., 2017). The boundaries of the marine isotope stages (MIS) Iberian Margin record and are projected in the Fucino record along the intercept points of the yellow/blue bars with the dashed green line, which is the linear interpolation between the mid-point of the tephra ages reported in Figure 9. The ages of Fucino tephras (dashed pink lines) are in turn projected in the time-scale of the Iberian Margin SST records, that are based on their own age models (Martrat et al., 2007; Rodrigues et al., 2011). The interceptions of the orange bars with the dashed green line also provide an age estimation for the Laschamp, Blake and Iceland Basin geomagnetic excursions, as inferred from the preliminary palaeomagnetic data.

Table 1: Analysed tephra layers from core F4-F5.

Fucino tephra	Sampling code	Bottom mcd	Thickness (cm)	Main lithological features	Source
TF-4	F5-8 77-93	**10.57**	15.50	Darkish coarse ash made of dense blackish porphyritic scoria including crystals of leucite, pyroxene and dark mica, also occurring as abundant loose clasts. Accessory lithic made of lava and holocrystalline clasts also occur.	Colli Albani
TF-5	F5-8 148-154	**11.13**	~6*	Darkish coarse ash made of dense blackish porphyritic scoria including crystals of leucite, pyroxene and dark mica, also occurring as abundant lose clasts. Accessory lithic made of lava and holocrystalline clast also occur.	Colli Albani
TF-7	F5-10 147-149	**14.14**	2.00	Greyish medium ash made of whitish-transparent micro-pumices associated with dense brownish glass shards with abundant lose crystals of large sanidine and black mica.	Ischia
TF-8	F5-12 90-95	**17.15**	4.50	Darkish ash made of blackish poorly vesicular scoria associated to scarce crystals of leucite and clinopyroxene.	Colli Albani
TF-12	F5-15 90-91	**21.53**	1.00	Greyish to dark yellow, fine grained ash with whitish-transparent micropumices and glass shards. Stretched/elongated vesicles, only very few loose crystals of sanidine, black mica and pyroxene.	Campi Flegrei-CVZ
TF-17	F5-20 89-91	**29.64**	2.00	Fine to coarse grained, greyish ash with 1) greyish dark vesicular scoria; 2) brownish and transparent glass shards and micropumice; 3) coarse, (rounded) whitish and greyish pumice, with loose sanidine, clinopyroxene, and amphibole crystals	Campi Flegrei-CVZ
TF-62	F4-39 90-100	**60,60**	10.00	Darkish coarse ash consisting of 1) greyish dark vesicular scoria; 2) brownish and transparent glass shards and micropumice; 3) coarse, (rounded) whitish and greyish pumice, with loose sanidine, clinopyroxene, and amphibole crystals.	Sabatini
TF-85	F5-49 74-88	**80.52**	13.25	Darkish medium-coarse ash made of both black porphyritic leucite-bearing scoriae and aphyric highly vesicular black scoriae, along with abundant crystals of leucite and dark mica and lithics. Toward the top, the ash becomes finer.	Colli Albani
TF-117	F5-57 0-7	**95.13**	7.00	Darkish fine ash made of black porphyritic leucite-bearing scoriae associated with free crystals of leucite and lithics. Toward the top, the sediment evolves into a coarse ash made of blackish vesicular porphyritic scoriae along with leucite and lithics.	Colli Albani
TF-118	F5-57 16-23	**95.29**	7.50	Darkish fine ash made of black porphyritic scoriae along with abundant free crystals of leucite and minor lithics.	Colli Albani
TF-126	F5-58 64-66	**97.24**	2.00	Light-grey medium ash made of highly vesicular white pumices associated with crystals of sanidine, plagioclase, dark mica and opaques and glass shards and minor lithics. Toward the top, the sediment turns to a dark grey-blackish medium ash.	Vulsini

*Base of tephra inside of the core-catcher, not in composite depth.

Supplementary materials

SD1: Full data set of the tephra glass major element composition (WDS-EMPA).

SD2: Full data set of the $^{40}Ar/^{39}Ar$ dating.

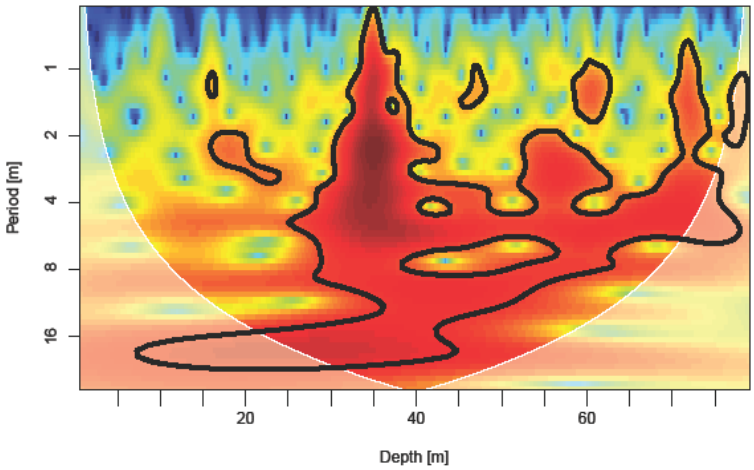

Figure S1. Wavelet analysis of the gamma ray dataset from F4 borehole. The white shading indicates areas outside the cone of influence that should be taken with care. Red colours indicate strong cyclicity, and blue colours no cyclic behaviour of the data. The bold line represents the results of a significance test, for details see Gouhier et al. (2018) and the appended R script.